Nuclear Science and Techniques (2024) 35:219
https://doi.org/10.1007/s41365-024-01583-2

Properties of QCD matter: a review of selected results from ALICE experiment

Qi-Ye Shou[1,2] · Yu-Gang Ma[1,2] · Song Zhang[1,2] · Jian-Hui Zhu[1,2] · Ya-Xian Mao[3] · Hua Pei[3] · Zhong-Bao Yin[3] · Xiao-Ming Zhang[3] · Dai-Cui Zhou[3] · Xin-Ye Peng[4] · Xiao-Zhi Bai[5] · Ze-Bo Tang[5] · Yi-Fei Zhang[5] · Xiao-Mei Li[6]

Received: 23 July 2024 / Revised: 27 September 2024 / Accepted: 1 October 2024 / Published online: 4 December 2024

Abstract
The Large Hadron Collider (LHC), the world's largest and most powerful particle accelerator, has been a pivotal tool in advancing our understanding of fundamental physics. By colliding heavy ions, such as lead ions, the LHC recreates conditions similar to those just after the Big Bang. This allows scientists to study the quark–gluon plasma (QGP), a state of matter in which quarks and gluons are not confined within protons and neutrons. These studies provide valuable insights into the strong force and the behavior of the early universe. In this paper, we present a comprehensive overview of recent significant findings from A Large Ion Collider Experiment (ALICE) at the LHC. The topics covered include measurements related to the properties of the QGP, particle production, flow and correlations, dileptons, quarkonia, and electromagnetic probes, heavy flavor, and jets. Additionally, we introduce future plans for detector upgrades in the ALICE experiment.

Keywords Relativistic heavy-ion collisions · Quark–gluon plasma · LHC · ALICE experiment

1 Introduction

The strong force dictates the interactions between quarks and gluons, the elementary particles responsible for most of the visible mass in the universe. Quantum chromodynamics (QCD), a non-Abelian gauge theory, provides the mathematical framework for describing the strong force and is crucial for comprehending the fundamental nature of matter under extreme conditions [1–3].

QCD is characterized by two notable features: asymptotic freedom and color confinement. Asymptotic freedom describes how the interaction between quarks and gluons weakens as their momentum exchange increases. Conversely, color confinement dictates that quarks and gluons cannot exist in isolation; they are always bound together within composite particles called hadrons, which cannot carry a net color charge and are the only observable entities. The field of "QCD condensed matter" investigates the

Dedicated to Professor Wenqing Shen in honour of his 80th birthday.

This work is supported in part by the National Key Research and Development Program of China (Nos. 2018YFE0104600, 2018YFE0104700, 2018YFE0104800, and 2018YFE0104900), the National Natural Science Foundation of China (Nos. 12061141008, 12147101, and 12322508), the Strategic Priority Research Program of Chinese Academy of Sciences (No. XDB34000000), and the Science and Technology Commission of Shanghai Municipality (23590780100).

✉ Qi-Ye Shou
shouqiye@fudan.edu.cn

[1] Key Laboratory of Nuclear Physics and Ion-Beam Application (MOE), Institute of Modern Physics, Fudan University, Shanghai 200433, China

[2] Shanghai Research Center for Theoretical Nuclear Physics, NSFC and Fudan University, Shanghai 200438, China

[3] Key Laboratory of Quark & Lepton Physics (MOE) and Institute of Particle Physics, Central China Normal University, Wuhan 430079, China

[4] School of Mathematics and Physics, China University of Geosciences (Wuhan), Wuhan 430074, China

[5] Department of Modern Physics, University of Science and Technology of China, Hefei, China

[6] China Institute of Atomic Energy, Beijing 102413, China

behavior of quarks and gluons in a dense, many-body system under conditions of high-energy density. By heating such a system, often with zero net baryon density, to temperatures above 150 − 160 MeV, scientists can observe the creation of quark–gluon plasma (QGP).

Unlike normal nuclear matter, the QGP is a state where quarks and gluons are not confined within hadrons. The early universe existed in this primordial state for the first few millionths of a second after the Big Bang, with the strong force playing a crucial role in the formation of the vast majority of visible mass in the universe. Recreating this primordial state of matter in laboratory experiments and studying its evolution can provide valuable insights into the organization of matter and the mechanisms that govern the confinement of quarks and gluons.

Relativistic heavy-ion collisions at the BNL-STAR generate QGP, which exists in extreme states characterized by being the hottest, densest, most vortical, and polarized, while also being the least viscous fluid ever studied in the laboratory [4–13]. The Large Hadron Collider—A Large Ion Collider Experiment (LHC-ALICE) heavy-ion collisions can generate even more extreme matter. The ALICE detector [14, 15] at the LHC was specifically designed to investigate the properties of QGP produced at these high energies. In the laboratory, conditions similar to those of the early universe can be recreated by colliding heavy ions at energies in the multi-TeV range. ALICE began physics data collection in 2009 with the first LHC pp collision at $\sqrt{s} =$ 0.9 TeV, and has since gathered data from all available collision systems and energies during Run 1 (2009–2013) and Run 2 (2015–2018). Notably, Pb–Pb collisions were studied in 2010 and 2011 at $\sqrt{s_{\rm NN}} = 2.76$ TeV, and in 2015 and 2018 at $\sqrt{s_{\rm NN}} = 5.02$ TeV. A brief run with Xe–Xe collisions at $\sqrt{s_{\rm NN}} = 5.44$ TeV took place in 2017. Proton–proton collisions at the same energies as Pb–Pb collisions were also conducted over the years, serving as a reference for nucleus–nucleus reactions and for specific QCD studies. To investigate cold nuclear matter effects, p–Pb collisions were studied in 2013 and 2016 at $\sqrt{s_{\rm NN}}$ =5.02 TeV and 8.16 TeV, following a pilot run in 2012. Additionally, ALICE collected pp collisions data at various energies up to $\sqrt{s} = 13$ TeV over the years. In 2021, ALICE completed a significant upgrade of its detectors to enhance its capabilities for scientific exploration during LHC Runs 3 and 4, planned until the end of 2032. Concurrently, plans are underway for ALICE 3, the next-generation experiment for LHC Runs 5 and 6.

The ALICE detector (Fig. 1) is positioned at the interaction point IP2 of LHC. It comprises a central barrel that covers the full azimuthal angle and pseudorapidity region $|\eta| < 0.9$. The detector is equipped with robust particle identification capabilities up to $p_{\rm T}$ of 20 GeV/c, along with excellent capabilities for reconstructing primary and secondary vertices. The main charged-particle tracking detectors of ALICE include the inner tracking system (ITS) and a large time projection chamber (TPC). Complementing the TPC, external tracking is provided by a transition radiation detector (TRD) and a time-of-flight system (TOF). Beyond the TOF, the azimuthal region houses two electromagnetic calorimeters: the high-resolution photon spectrometer

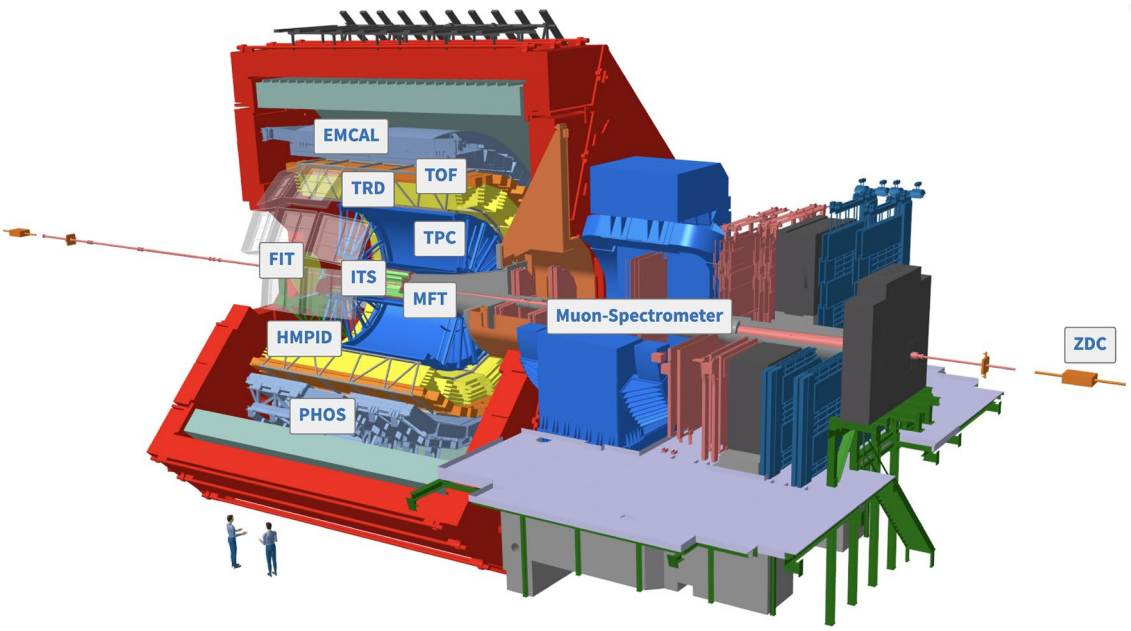

Fig. 1 (Color online) ALICE detector in Run 3 era. See text for details

(PHOS) and EMCal, as well as a high momentum particle identification detector (HMPID). The central barrel detectors are enclosed within the L3 solenoid magnet, which generates a magnetic field of up to $B = 0.5$ T. In the forward region, ALICE has a muon spectrometer and various sets of smaller detectors, including the forward multiplicity detector (FMD), photon multiplicity detector (PMD), V0, T0, and zero-degree calorimeters (ZDC). Each year, the data collected at ALICE can easily reach sizes exceeding tens of petabytes. Processing such vast amounts of data for reconstructing physics objects from raw data is made possible by the worldwide LHC computing grid (WLCG) infrastructure, which relies on approximately 200 computing clusters distributed worldwide. In China, a newly reactivated cluster located at the Institute of High Energy Physics, CAS, Beijing, has been operational since 2024.

Below, we provide a brief introduction to selected physics topics investigated by ALICE, organized as follows: In Sect. 2, we present highlights on macroscopic properties 2.1, flow and correlations 2.2, dileptons, quarkonia, and electromagnetic probes 2.3, heavy flavor 2.4, and jets 2.5. Future plans for detector upgrades have been discussed in Sect. 3.

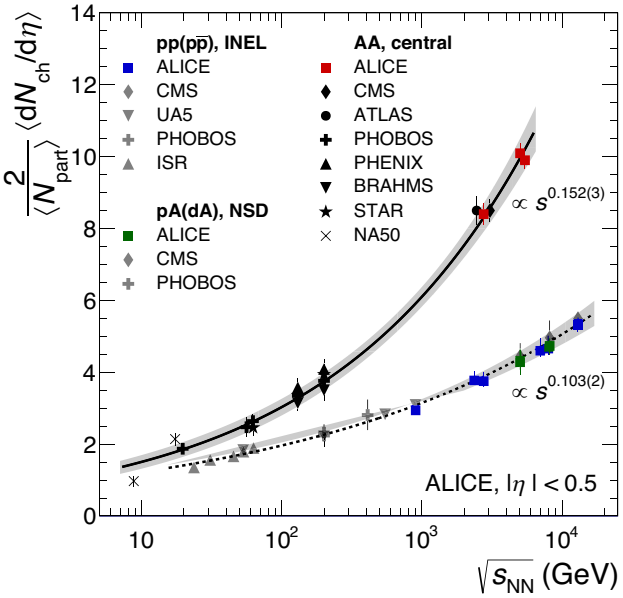

Fig. 2 (Color online) Collision energy dependence of charged-particle pseudorapidity density at midrapidity ($|y|$<0.5) normalized to average number of participants, $\frac{2}{\langle N_{\rm part}\rangle}\langle {\rm d}N_{\rm ch}/{\rm d}\eta\rangle$

2 Study of quark–gluon plasma

2.1 Macroscopic properties

Objective of the ALICE is to investigate the QGP created at center-of-mass energies ranging from a few TeV. A crucial aspect of this research is estimating the initial energy density and temperature necessary for QGP formation in collisions. The initial energy density can be inferred from the observed hadron production in the final state of the fireball across different collision centrality classes and at varying center-of-mass energies. Figure 2 from [15] illustrates the scaled charged-particle multiplicity measured at midrapidity ($|y| < 0.5$), normalized by $\langle N_{\rm part}\rangle/2$, in various collision systems, including pp, p$\bar{\rm p}$, p(d)A, and central heavy-ion collisions, plotted against the center-of-mass energy per nucleon pair, $\sqrt{s}$. ALICE has contributed data from Pb–Pb collisions at $\sqrt{s_{\rm NN}} = 2.76$ TeV and 5.02 TeV, Xe–Xe collisions at $\sqrt{s_{\rm NN}} = 5.44$ TeV, and pp(p̄, Pb) collisions spanning a broad range of $\sqrt{s}$ from the TeV range to above 10 TeV. The dependence of $\frac{2}{\langle N_{\rm part}\rangle}\langle\frac{{\rm d}N_{\rm ch}}{{\rm d}\eta}\rangle$ on $\sqrt{s_{\rm NN}}$ was fitted with a function of $\alpha \times s^{\beta}$. The fitting results yielded $\beta = 0.152 \pm 0.003$ for central A–A collisions and $\beta = 0.103 \pm 0.002$ for p–p and p(d)–A collisions. This indicates that heavy-ion collisions are significantly more efficient in converting initial beam energy into particle production at midrapidity compared to pp or p–Pb collisions [15].

The size dependence of particle production in collision systems ranging from p-p(Pb) to Xe–Xe and Pb–Pb has been measured with unprecedented precision. Figure 3 from [15] illustrates the centrality dependence of $\langle N_{\rm part}\rangle$ on $\frac{2}{\langle N_{\rm part}\rangle}\langle\frac{{\rm d}N_{\rm ch}}{{\rm d}\eta}\rangle$. Data were collected from Pb–Pb and Xe–Xe collisions at $\sqrt{s_{\rm NN}} = 5.02$ TeV and 5.44 TeV, respectively, as well as from Au–Au and Cu–Cu collisions at RHIC energy setups. Uncertainties range from approximately 3% for central A–A collisions at midrapidity to approximately 10% for peripheral results in the forward region. Results at $\sqrt{s_{\rm NN}} = 5.02$ TeV were scaled using factors calculated from the fit function in Fig. 2 for the top 5% most central Au–Au, Cu–Cu, and Xe–Xe collisions. At the same $\langle N_{\rm part}\rangle$, the shape of $\frac{2}{\langle N_{\rm part}\rangle}\langle\frac{{\rm d}N_{\rm ch}}{{\rm d}\eta}\rangle$ as a function of $\langle N_{\rm part}\rangle$ exhibited slightly more variability in Xe–Xe compared to Pb–Pb, with a similar pattern observed between Au–Au and Cu–Cu collision systems. Reference [15] noted that these deviations, while present, are not significant given the large uncertainties, and could be attributed to the different Glauber model simulations used to estimate $\langle N_{\rm part}\rangle$ in ALICE [16] and RHIC [17]. Comparison to PYTHIA 8.3 [18] calculations in Fig. 3, with different centrality selection methods (e.g., $N_{\rm ch}$-selected and $N_{\rm part}$-selected), revealed variations in the dependence of $\frac{2}{\langle N_{\rm part}\rangle}\langle\frac{{\rm d}N_{\rm ch}}{{\rm d}\eta}\rangle$, sug-

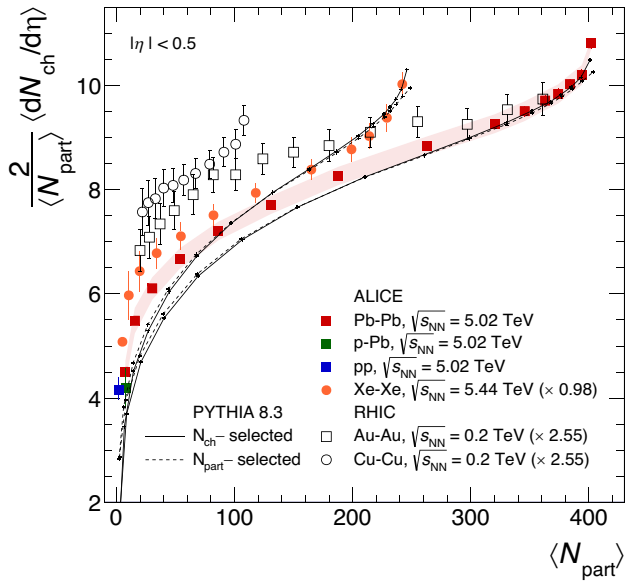

Fig. 3 (Color online) Values of $\frac{2}{\langle N_{\rm part}\rangle}\langle {\rm d}N_{\rm ch}/{\rm d}\eta\rangle$ are compared in various collisions

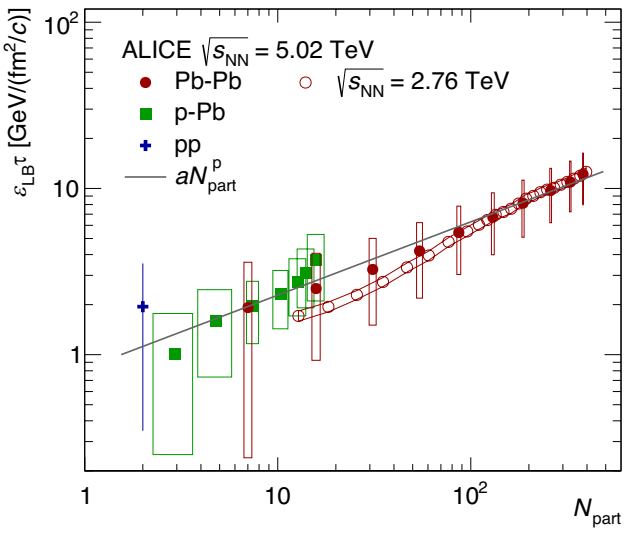

Fig. 4 (Color online) Lower-bound estimate of the energy density times the formation time τ in pp, p–Pb, and Pb–Pb collisions at $\sqrt{s_{\rm NN}}$ = 5.02 TeV as a function of the number of participants [30]

gesting fluctuations in charged-particle multiplicity at a fixed number of particle sources.

Particle production measurements are pivotal in estimating the initial energy density and temperature, which are crucial for determining whether the conditions for the QCD phase transition are met during collisions [19–26]. The energy density in the collision can be estimated using the "Bjorken estimate" [27]: $\epsilon(\tau)$, which is derived from the total produced transverse momentum. This estimation method applies to a system that undergoes free-streaming with boost-invariant longitudinal expansion and no transverse expansion, as described in references [15, 27]. By using the measured charged-particle pseudorapidity density and assuming a normal distribution of charged particles in rapidity [28, 29], it becomes feasible to derive a lower-bound estimate of the energy density $\varepsilon_{\rm LB}$ multiplied by the formation time τ in the collisions [30]. The transverse area $S_{\rm T}$ is determined using the Glauber model [31], which accounts for all participating nucleons. Figure 4 illustrates the resulting product $\varepsilon_{\rm LB}\tau$ for pp, p–Pb, and Pb–Pb collisions at $\sqrt{s_{\rm NN}} = 5.02$ TeV, as well as Pb–Pb collisions at $\sqrt{s_{\rm NN}} = 2.76$ TeV. A power-law fit $aN_{\rm part}^{\rm p}$ applied to the data indicates a significant increase in the energy density with the increase in transverse area of the initial overlap between the colliding nuclei [15].

Another critical parameter in determining the formation of QGP is the temperature of the system created in collisions. It is important to distinguish between two concepts of temperature: the chemical freeze-out temperature [32] and the kinetic freeze-out temperature [33]. These temperatures characterize the thermodynamic properties of the fireball at the stages of chemical equilibrium and ceasing of hadron rescattering, respectively. The measurement of the kinetic freeze-out temperature has incorporated light nuclei to explore the system's thermalization [34]. Owing to their large mass, (anti-)α production yields and transverse-momentum spectra are particularly significant as they rigorously test particle production models. The combined anti-α and α spectrum, when included in a common blast-wave fit with lighter particles, indicates that the (anti-)α also participates in the collective expansion of the collision medium. A blast-wave fit using only protons, (anti-)α, and other light nuclei yields a flow velocity comparable to that from a fit including all particles. However, fitting only protons and light nuclei results in a similar flow velocity but a notably higher kinetic freeze-out temperature, as shown in Fig. 5. Interestingly, hypernuclei exhibit a similar flow velocity and kinetic freeze-out temperature to light nuclei [35, 36], although more data from ALICE Run 3 is needed to solidify these findings [35].

The temperature of the early partonic phase can be experimentally accessed through sensitive probes produced in the early stages of collisions, such as heavy-flavor q$\bar{\rm q}$ states (quarkonia) and electromagnetic radiation. Since the seminal work by Matsui and Satz [39], quarkonium has been proposed as a thermometer for the QGP. The strong binding potential between quark and antiquark pairs is screened by color charges in the dense and hot medium, leading to the "melting" of q$\bar{\rm q}$ states. This phenomenon offers the opportunity to correlate the production or suppression of quarkonia with the temperature of the QGP. A detailed discussion on quarkonia and dileptons will be presented in Sect. 2.3.

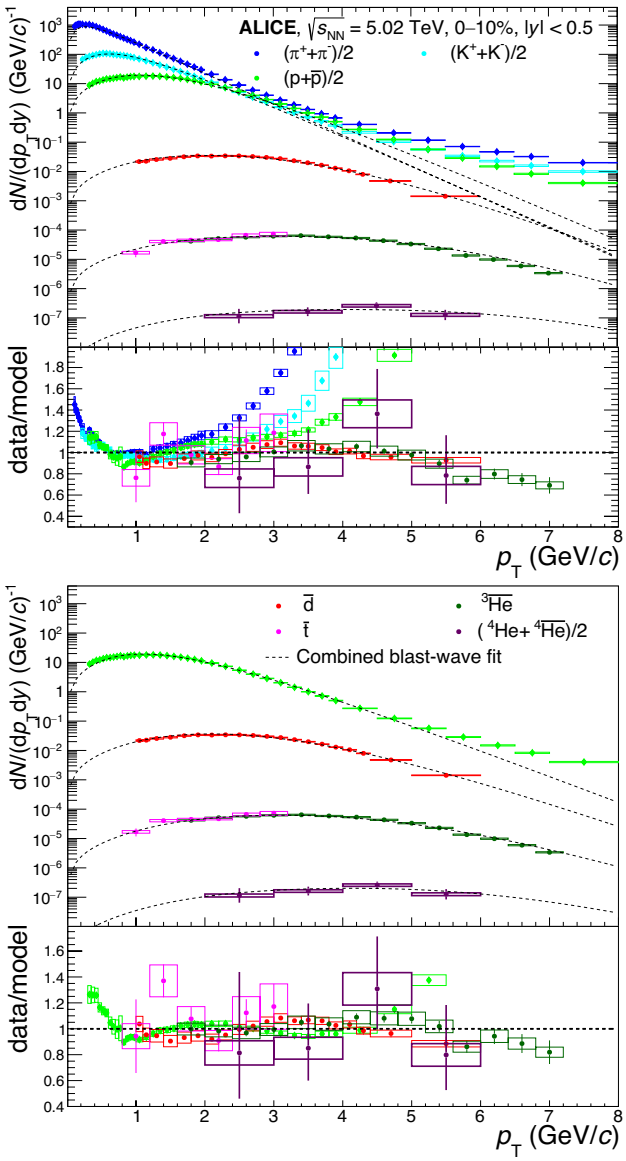

Fig. 5 (Color online) Combined blast-wave fit of all available light flavored hadron p_T spectra including nuclei [37, 38] (left) and only p, $\bar{d}$, $\bar{t}$, $^3\overline{He}$, and ^{4}He p_T spectra (right) in Pb–Pb collisions at $\sqrt{s_{NN}} = 5.02$ TeV for 0%–10% central events (upper panels). Lower panels show ratio between each data point and blast-wave model fit for each species

The temperature can be experimentally accessed through the measurement of thermal photons emitted by the hot plasma, as their production rate provides insights into the early conditions of the QGP. Direct photons are those that do not originate from parton fragmentation or hadronic decays but are instead produced by electromagnetic interactions during various stages of the collision. Figure 6 presents the direct photon spectra measured in Pb–Pb collisions at 2.76 TeV by the ALICE collaboration [40] and in Au–Au collisions at 0.2 TeV by the PHENIX collaboration [41, 42] in the 0–20% and 20–40% centrality classes. Thermal photons dominate the low transverse-momentum region ($p_T \lesssim 3$ GeV/c), following an approximately exponential behavior characterized by $d^2N_{\gamma_{dir}}/(p_T dp_T dy) \propto e^{-p_T/T_{eff}}$. The inverse logarithmic slope T_{eff} accounts for the radial expansion of the system, causing a blue-shift of emitted photons [45]. At higher momenta ($p_T \gtrsim 5$ GeV/c), the direct photon spectrum includes contributions from "prompt" photons, which originate from initial hard scatterings and the subsequent interaction of hard scattered partons with the medium (referred to as "jet-photon conversion"). The invariant yield of direct photons is determined by first measuring the excess of direct photons over decay photons, denoted by R_γ. Figure 6 presents R_γ for central and semi-central Pb–Pb collisions at = 2.76 TeV. At high momenta ($p_T \gtrsim 5$ GeV/c), the ratio R_γ indicates consistency with prompt photon production predicted by perturbative quantum chromodynamics (pQCD) and JETPHOX calculations [46, 47]. The excess of direct photons observed at low transverse momentum (0.9 GeV/c < p_T < 2.1 GeV/c) suggests an abundance of thermal photons originating from the quark–gluon plasma (QGP). This region, dominated by thermal direct photons, is fitted with an exponential function to extract the effective temperature (T_{eff}), yielding values of $T_{eff} = (304 \pm 41)$ MeV and $T_{eff} = (407 \pm 114)$ MeV for central and semi-central Pb–Pb collisions, respectively. Comparing these temperatures to the slopes of the spectra measured by PHENIX, an increase in the effective temperature from RHIC to the LHC is evident. However, directly determining the initial temperature of the fireball remains challenging and has not yet been achieved, as it requires model calculations that account for the evolution of the QGP medium and radial flow effects, as discussed in [15].

The system size and lifetime are crucial indicators of the fireball properties created in collisions, assessed through particle momentum correlations, known as femtoscopy, at the final kinetic freeze-out state. Historically referred to as "HBT interferometry" after its originators Hanbury-Brown and Twiss in the 1950 s and 1960 s in astronomy [48, 49], femtoscopy involves constructing relative momentum correlations and fitting them to extract particle interaction and source parameters (see Sect. 2.2). The volume measured by femtoscopy corresponds to the size of the emitting source, known as the homogeneity volume, which typically differs from the total volume of the system at freeze-out [50].

The upper portion of Fig. 7 illustrates how the size of the homogeneity region, inferred from femtoscopic pion radii, scales with the charged-particle pseudorapidity density. These measurements were conducted in central p–Pb and Au–Au collisions across various energy regimes. Notably, the size of the homogeneity region increases approximately threefold from AGS energies to the LHC [15]. The decoupling time of the system is commonly approximated using the decoupling time of pions, τ_f, owing to their predominant

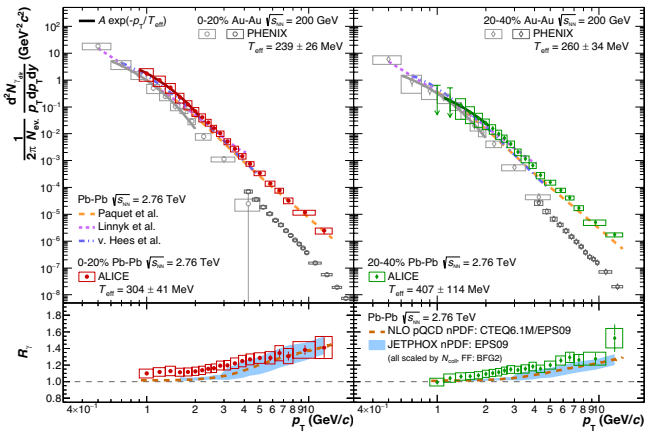

Fig. 6 (Color online) Direct photon spectra (top) and direct photon excess R_γ (bottom) measured in Pb–Pb collisions at 2.76 TeV [40] and in Au–Au collisions at 0.2 TeV [41, 42] in 0%–20% (left) and 20–40% (right) centrality classes

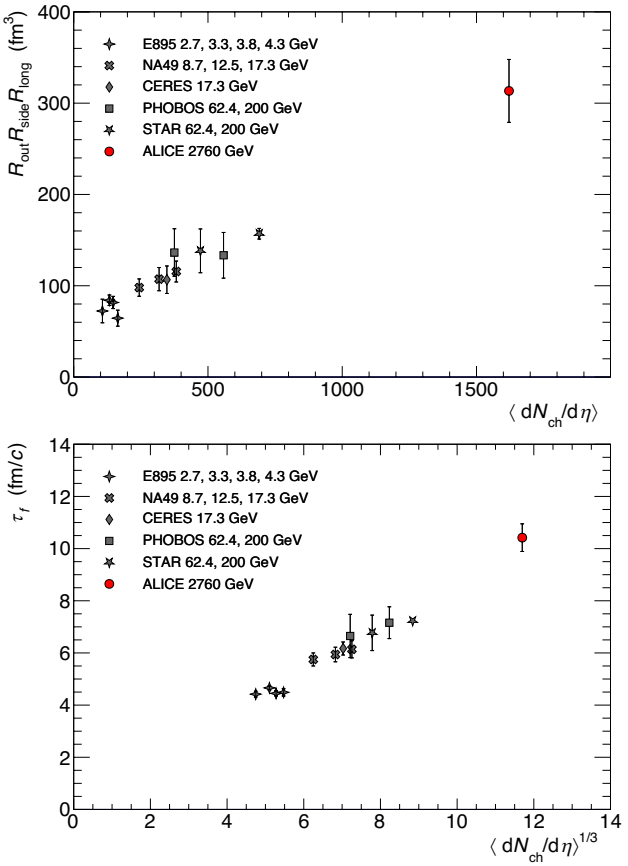

Fig. 7 (Color online) Homogeneity volume (top) and decoupling time τ_f (bottom) measured at 2.76 TeV [43, 44] compared to those obtained at experiments at lower energies. Homogeneity region is determined as product of three pion femtoscopic radii at $\langle k_T \rangle$ = 0.3 GeV/c for 0–5% central events

abundance (approximately 80%) within the system. The lower panel of Fig. 7 illustrates τ_f alongside global data. It shows a linear increase with the cube root of the charged-particle pseudorapidity density, starting from 4–5 fm/c at AGS energies, rising to 7–8 fm/c at the highest RHIC energies, and reaching 10–11 fm/c in central Pb–Pb collisions at $\sqrt{s_{NN}}$ =2.76 TeV.

2.2 Flow and correlations

The dynamic behavior of the QGP provides crucial insights into strongly interacting matter. These properties are primarily defined by measurements of the collective motion of final-state particles generated in heavy-ion collisions. Anisotropic flow, quantified by Fourier coefficients of the particle azimuthal distributions with respect to symmetry plane angles, Ψ, is a key observable. A cornerstone in exploring the strongly coupled QGP paradigm involves extensive measurements of elliptic flow (v_2) and triangular flow (v_3), the second- and third-order components of anisotropic flow, respectively. Characteristic features of v_2 measurements include mass ordering, particle species grouping (e.g., mesons and baryons), and number of constituent quarks (NCQ) scaling. These features can be interpreted as the interplay between the dominant ellipsoidal geometry in the initial state, the collective expansion of the system, and hadronization through quark coalescence. Overall, these measurements suggest the creation of an "ideal fluid" in relativistic heavy-ion collisions.

Beyond measuring v_2, studying v_2 fluctuations can provide deeper insights into the collective behavior of the QGP. In [52], the elliptic flow of identified hadrons in Pb–Pb collisions at $\sqrt{s_{NN}}$ = 5.02 TeV is measured using two- ($v_2\{2\}$) and four- ($v_2\{4\}$) particle cumulants. By combining data for both $v_2\{2\}$ and $v_2\{4\}$, ALICE presents the first measurements of mean elliptic flow, elliptic flow fluctuations, and relative elliptic flow fluctuations for various hadron species, probing event-by-event eccentricity fluctuations in the initial state as well as contributions from the dynamic evolution of the expanding QGP. When compared with hydrodynamic calculations incorporating quark coalescence, differences in the relative flow fluctuations for different particle species are observed, suggesting

that final-state hadronic interactions further modify these fluctuations.

The correlations between event-by-event fluctuations of two different flow amplitudes are commonly quantified using "symmetric cumulant" (SC) observables. Building on previous measurements [53], ALICE has extended event-by-event correlations to include three flow amplitudes in higher-order SC observables [54]. These three-harmonic correlations emerge during the collective evolution of the medium and differ from those present in the initial state, which cannot be explained by previous lower-order flow measurements. They provide the first constraints on the nonlinear response contribution in v_5 from v_2 and v_3, enhancing our understanding of the event-by-event flow fluctuation patterns in the QGP.

In recent years, striking similarities between numerous observables, including the "ridge" structure, have been observed in A–A and high-multiplicity p-A and pp collisions at both RHIC and LHC energies, revealing the presence of collectivity in small-system collisions. To investigate the "smallest" (p-A, pp, ee...) and "dilutest" (lower multiplicity) limit of collectivity onset, various measurements are performed in ALICE. In [51], flow coefficients and their cross-correlations using two- and multiparticle cumulants are studied and compared in collisions of pp at $\sqrt{s} = 13$ TeV, p–Pb at $\sqrt{s_{\rm NN}} = 5.02$ TeV, Xe–Xe at $\sqrt{s_{\rm NN}} = 5.44$ TeV, and Pb–Pb at $\sqrt{s_{\rm NN}} = 5.02$ TeV, as shown in Fig. 8. The multiplicity dependence of v_n is measured over a wide range. An ordering of the coefficients $v_2 > v_3 > v_4$ is observed in pp and p–Pb collisions, similar to that seen in large collision systems. However, a weaker v_2 multiplicity dependence is found compared to A–A collisions within the same range. In Fig. 9, the v_2 measurements for charged π, K, and p are presented and compared with state-of-the-art Hydro-Coal-Frag calculations incorporating quark coalescence [55]. A characteristic grouping and splitting of v_2 for baryons and mesons is observed. The NCQ scaling is further examined and found to approximately hold [56], as shown in Fig. 10. These results collectively confirm the existence of partonic collectivity.

In Ref. [51], a novel subevent method is employed, revealing that v_2 measured with four-particle cumulants aligns well with that from six-particle cumulants in pp and p–Pb collisions. The correlation magnitude between v_n^2 and v_m^2, assessed with the aforementioned SC, is consistently positive across all multiplicities for v_2 and v_4. Conversely, for v_2 and v_3, the correlation is negative and changes sign at low multiplicity, indicating a different fluctuation pattern for v_n.

The measurement of near-side associated per-trigger yields (ridge yields) from the analysis of angular correlations of charged hadrons is performed in pp collisions at $\sqrt{s} = 13$ TeV [57]. A prominent jet-fragmentation peak, resulting from the correlations of particles originating from the fragmentation of the same parton, is clearly observed.

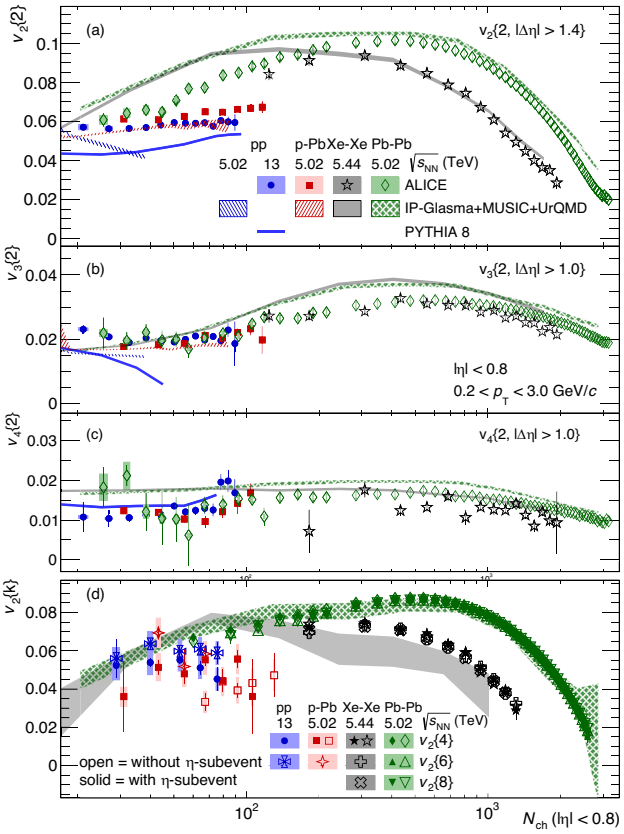

Fig. 8 (Color online) Multiplicity dependence of v_n for pp, p–Pb, Xe–Xe, and Pb–Pb collisions. [51]

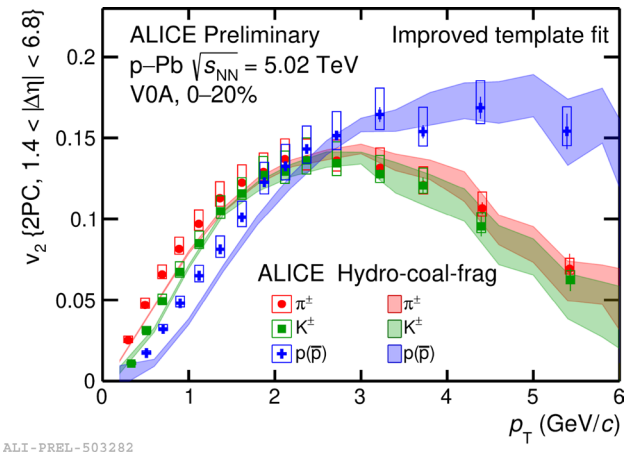

Fig. 9 (Color online) $p_{\rm T}$-differential v_2 measured with two-particle correlation for various hadrons in p–Pb collisions at $\sqrt{s_{\rm NN}} = 5.02$ TeV is compared with calculations from the Hydro-Coal-Frag model. [55]

A broad away-side structure emerges from the correlations of tracks from back-to-back jet fragments, spreading across the entire $\Delta\eta$ region. As illustrated in Fig. 11, an enhancement of the correlation, known as the "ridge" structure, is

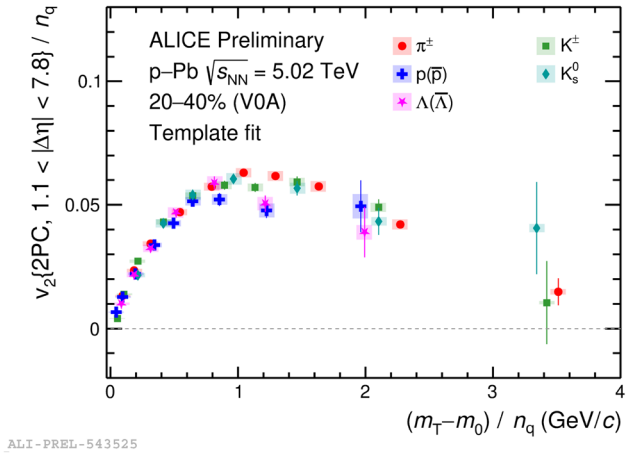

Fig. 10 (Color online) The NCQ scaling for various baryons and mesons measured in p–Pb collisions at $\sqrt{s_{NN}}$ = 5.02 TeV, indicating the existence of partonic collectivity. [56]

visible at $|\Delta\eta| > 1.4$ and $\Delta\phi = 0$. This ridge, observed in previous measurements, is interpreted in heavy-ion collisions as indicative of the collective expansion of the QGP medium. Long-range ridge yields are extracted, extending into the low-multiplicity region where a strongly interacting medium is typically unlikely to form. The precision of these new low-multiplicity results enables the first direct quantitative comparison with results obtained in e^+e^- collisions, as shown in Fig. 12. In e^+e^- collisions, initial-state effects such as preequilibrium dynamics and collision geometry are not expected to play a role. In the multiplicity range where the e^+e^- results are precise, ridge yields in pp collisions are

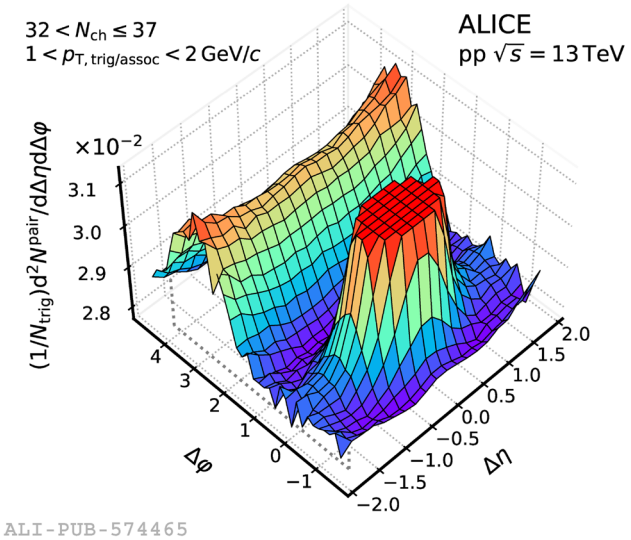

Fig. 11 (Color online) Two-particle per-trigger yield measured for charged track pairs within multiplicity range $32 < N_{ch} < 37$. Jet-fragmentation peak has been truncated for better visibility. [57]

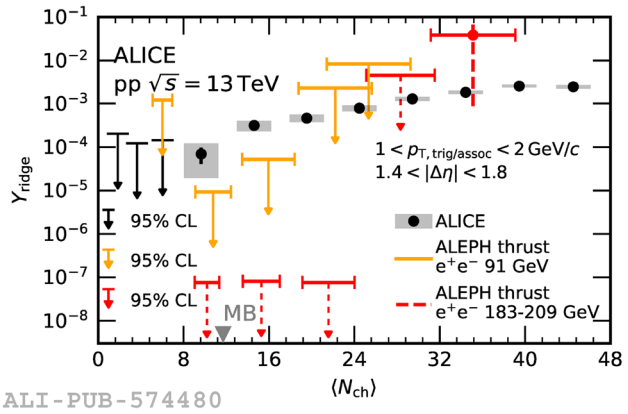

Fig. 12 (Color online) Ridge yield as a function of multiplicity, compared to the upper limits on the ridge yield in e^+e^- collisions. [57]

substantially larger than those observed in e^+e^- annihilations, indicating that the processes involved in e^+e^- annihilations do not significantly contribute to the emergence of long-range correlations in pp collisions.

The study of nuclear structure in heavy-ion collisions has drawn extensive attention in recent years. Pearson correlations between mean transverse momentum [p_T] and v_2 (v_3) are measured as a function of centrality in Pb–Pb (spherical) and Xe–Xe (deformed) collisions at 5.02 and 5.44 TeV, respectively, in ALICE [58, 59]. The positive correlations of $\rho(v_2^2, [p_T])$ and $\rho(v_3^2, [p_T])$, along with the negative higher-order correlation, are well explained by hydrodynamic models with IP-Glasma initial conditions. This suggests that geometric effects in the initial state play a significant role. The data obtained from Xe–Xe collisions provide a novel avenue for investigating nuclear structure through relativistic heavy-ion collisions at the LHC. Further studies can be found in [60].

Heavy-ion collisions generate extremely strong electromagnetic fields, predominantly caused by spectator protons. These fields are estimated to reach magnitudes of 10^{18}–10^{19} Gauss within the first 0.5 fm of the collision at LHC energy levels. In Ref. [61, 62], such strong electromagnetic fields are probed through charge-dependent directed flow (v_1) [63] in Pb–Pb collisions at $\sqrt{s_{NN}}$ = 5.02 TeV. The difference in v_1 between positively and negatively charged hadrons exhibits a positive slope with respect to η. Measurements for D^0 mesons and their anti-particles reveal a value three orders of magnitude greater than that for charged hadrons. This significant disparity provides new insights into the effects of the strong electromagnetic field, the initial tilt of matter, and the differing sensitivities of charm and light quarks to the early dynamics of heavy-ion collisions. The interplay between the chiral anomaly and intense magnetic (vortical) fields is suggested to generate several chiral anomalous effects [64–67], such as the chiral magnetic effect (CME),

Table 1 Fractions and upper limits of CME and CMW signals measured at ALICE

	Dataset	Fraction	Upper limit (%)
CME	Pb–Pb 2.76 TeV [70]	−2.1%±4.5%	15
	Pb–Pb 5.02 TeV [70]	0.3%±2.9%	18
	Pb–Pb 5.02 TeV [71]	15%±6%	25
	Xe–Xe 5.44 TeV [71]	−0.1%±1%	2
CMW	Pb–Pb 5.02 TeV [72]	8%±5%	26

chiral magnetic wave (CMW), and chiral vortical effect (CVE). Utilizing various azimuthal- and charge-dependent correlators and methods, the fractions and upper limits (at 95% C.L.) of the CME and CMW have been experimentally extracted with unprecedented precision, as listed in Table 1. Notably, the CMW fraction is a pioneering achievement among all experiments, and a unified background of Local Charge Conservation (LCC) intertwined with collective flow is further proposed to simultaneously interpret the CME and CMW measurements [68]. The chiral vortical effect has also been experimentally measured using Λ-p pairs [69].

In addition to azimuthal correlations, ALICE serves as a novel laboratory for determining the space–time characteristics of relativistic heavy-ion collisions and hadron–hadron interactions through momentum correlations [74, 75]. In Ref. [73], momentum correlations between hyperon–proton pairs are measured in $\sqrt{s}$ =13 TeV pp and $\sqrt{s_{\rm NN}}$ =5.02 TeV p–Pb collisions with high precision. The influence of strong interactions is examined by comparing experimental data with lattice calculations. In Fig. 13, it is observed that the signal for p-Ω^- pairs is up to twice as large as that for p-Ξ^- pairs. The measured correlations exhibit significant enhancement compared to the Coulomb prediction, indicating the presence of an additional strong attractive interaction. In Ref. [76], p − Λ correlations are measured in $\sqrt{s} = 13$ TeV pp collisions. The significance of the coupling between p − Λ and $N - \Sigma$ is evident from a cusp-like enhancement observed at the corresponding threshold energy. This marks the first direct experimental observation, offering an opportunity to refine theoretical calculations for the coupled $N - \Sigma \leftrightarrow N - \Lambda$ system. In another study, Ref. [77] investigates the p-Σ^0 interaction directly, reconstructing Σ^0 through the $\Lambda\gamma$ channel. The measured results suggest a shallow strong interaction. In Ref. [78], p-ϕ correlations are obtained from $\sqrt{s} = 13$ TeV pp collisions. By fitting the data with theoretical calculations, the scattering length and effective range are extracted. The measured results conclusively exclude inelastic processes in the p-ϕ interaction, providing valuable experimental data for achieving a self-consistent description of the N-ϕ interaction.

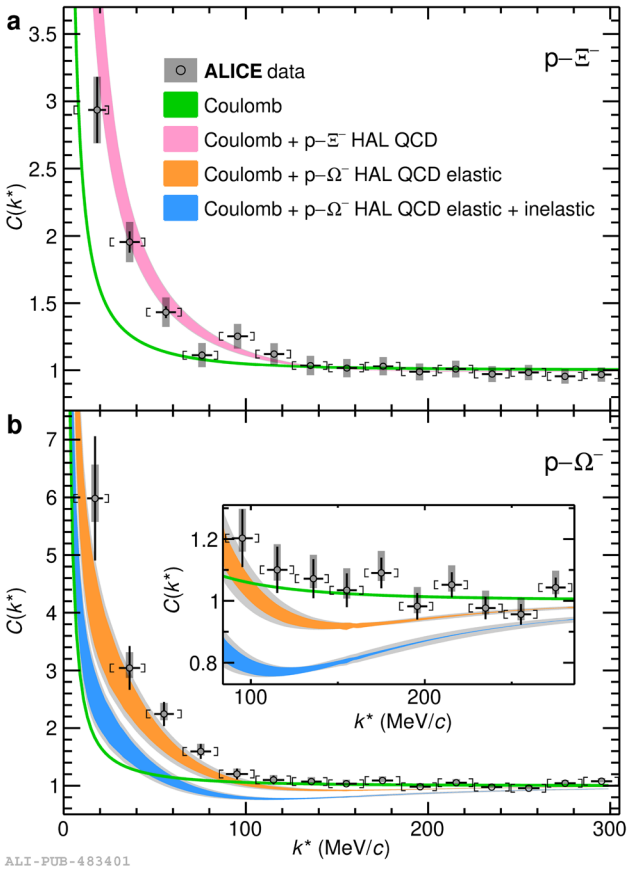

Fig. 13 (Color online) Experimental p-Ξ^- and p-Ω^- correlation functions, indicating the presence of additional strong attractive interaction. [73]

In Ref. [80], kaon–proton correlations are measured in $\sqrt{s} = 13$ TeV pp collisions, both near and above the kinematic threshold. A significant structure is observed around a relative momentum of 58 MeV/c in the correlation function of opposite-charge Kp pairs. This observation, with high statistical significance, represents the first experimental evidence for the opening of the neutral Kn isospin-breaking channel, providing the most precise experimental information to date on the KN interaction.

In the search for the possible Λ-Λ bound state, known as the H-dibaryon, femtoscopic correlations of Λ-Λ pairs are studied in pp and p–Pb collisions [79]. By comparing measured data with model calculations, the scattering parameter space, characterized by the inverse scattering length and effective range, is constrained in Fig. 14. The data reveal a shallow attractive interaction, consistent with findings from hypernuclei studies and lattice computations.

In addition to strange hadrons, similar measurements have also been extended to charm hadrons. In Ref. [81], momentum correlations of p-D^- and their anti-particle pairs are measured in $\sqrt{s}$ =13 TeV collisions. The data are

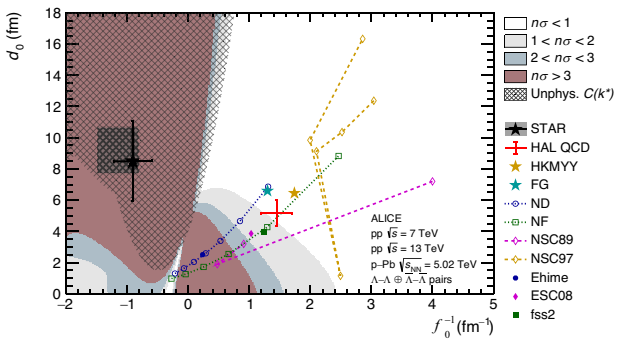

Fig. 14 (Color online) Exclusion plot for the Λ-Λ scattering parameters. Different colors represent the confidence level of excluding a set of parameters. [79]

consistent with either a Coulomb-only interaction hypothesis or a shallow N-d strong interaction, contrary to predictions of a repulsive interaction. In Ref. [82], various π-d and K-d pairs are also studied. For all particle pairs, the data can be adequately described by Coulomb interaction alone, and the extracted scattering lengths are consistent with zero. This suggests a shallow interaction between charm and light-flavor mesons.

Three-body nuclear forces are crucial for understanding the structure of nuclei, hypernuclei, and the dynamics of dense baryonic matter, such as in neutron stars. In Ref. [83], ALICE presents the first direct measurement of three-particle correlations involving p-p-p and p-p-Λ systems in pp collisions at $\sqrt{s}$ =13 TeV. Using the Kubo formalism, three-particle cumulants are extracted from the correlation functions, where the contribution of the three-particle interaction is isolated by subtracting known two-body interaction terms. A negative cumulant is observed for the p-p-p system, suggesting the presence of a residual three-body effect. Conversely, the cumulant for the p-p-Λ system is consistent with zero, indicating no significant three-particle correlations in this case. Studying correlations between a given particle species and deuterons (d) offers an alternative approach to exploring three-body interactions, as deuterons are composed of a neutron and a proton. In Ref. [84], K^+-d and p-d femtoscopic correlations are measured. The relative distances at which deuterons and p/K^+ are produced are approximately 2 fm. Importantly, only a full three-body calculation that considers the internal structure of the deuteron can adequately explain the observed data. These measurements demonstrate the feasibility of probing three-body correlations at the LHC, providing valuable insights into the complex dynamics involving nuclei and their constituents.

2.3 Dileptons, quarkonia, and electromagnetic probes

Heavy quarkonia, which are bound states of charm-anticharm (charmonium) or bottom-antibottom (bottomonium) pairs, have been extensively studied in various experiments. Quarkonia serve as essential probes for studying the QGP and its properties. The binding of heavy-quark pairs is affected by the screening of the QCD force due to the high density of free color charges in the QGP, leading to quarkonium dissolution. This concept was first proposed in 1986 [39], with initial studies aiming to link quarkonium suppression directly to the temperature of the deconfined phase. The binding energies of quarkonia, which range from a few MeV to over 1 GeV, suggest a "sequential suppression" with increasing temperature, where strongly bound states persist up to higher dissociation temperatures. In nuclear collisions, varying the QGP temperature by adjusting collision centrality or energy could potentially make quarkonia an ideal thermometer for the medium.

The nuclear modification factor ($R_{\rm AA}$) is calculated using the measured yields from Pb–Pb and pp collisions at the same center-of-mass energies. Figure 15 presents the $p_{\rm T}$ -integrated J/ψ $R_{\rm AA}$ as a function of $N_{\rm part}$ in Pb–Pb collisions at $\sqrt{s_{\rm NN}}$ = 5.02 TeV [85, 86]. J/ψ produced via photo-production processes [87, 88], particularly in peripheral collisions [89, 90], are excluded by applying $p_{\rm T}$ thresholds greater than 0.15 GeV/c at midrapidity and greater than 0.3 GeV/c at forward rapidity.

A strong suppression of the J/ψ $R_{\rm AA}$ is observed in semi-central and central Pb–Pb collisions, especially at forward rapidity. At midrapidity, $R_{\rm AA}$ exhibits a slight increasing trend from semi-central to central collisions, with $R_{\rm AA}$ values at midrapidity being slightly larger than those at forward rapidity. This difference is statistically significant, showing a 2.2σ deviation in the 0–10% centrality interval. The larger $R_{\rm AA}$ in central collisions at midrapidity provides strong evidence for (re)generation effects of J/ψ production at LHC energies [91–93].

The production of the $\psi(2S)$ was measured in Pb–Pb collisions at $\sqrt{s_{\rm NN}}$ = 5.02 TeV, with $p_{\rm T}$ down to 0 for the first time at LHC energies, utilizing the dimuon decay channel at forward rapidity ($2.5 < y < 4$) by the ALICE experiment [95]. The nuclear modification factors $R_{\rm AA}$ of $\psi(2S)$ and J/ψ are compared as a function of $N_{\rm part}$ in the upper panel of Fig. 16. The $R_{\rm AA}$ values for $\psi(2S)$ are systematically lower than those for J/ψ. The results are compared with calculations from a microscopic transport model [94] and the statistical hadronization model [91]. The agreement between the data and the transport model is slightly better than with the statistical hadronization model, particularly for $\psi(2S)$.

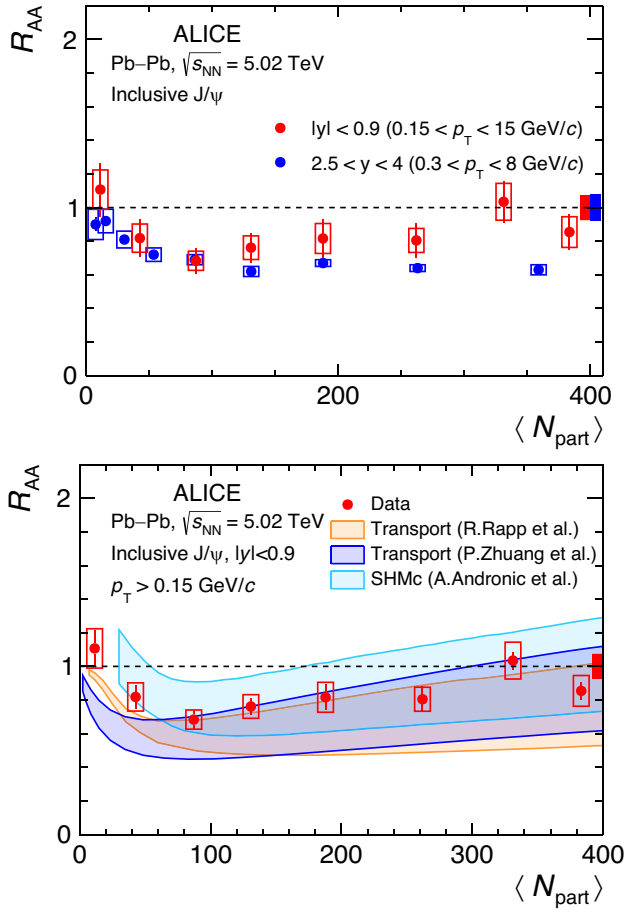

Fig. 15 (Color online) p_T-integrated inclusive J/ψ R_{AA} at midrapidity and forward rapidity, as a function of number of participants in Pb–Pb collisions at $\sqrt{s_{NN}}$ = 5.02 TeV (upper panel) [86], R_{AA} at midrapidity are compared with calculations from two microscopic transport models [92, 94] and statistical hadronization model [91] (lower panel)

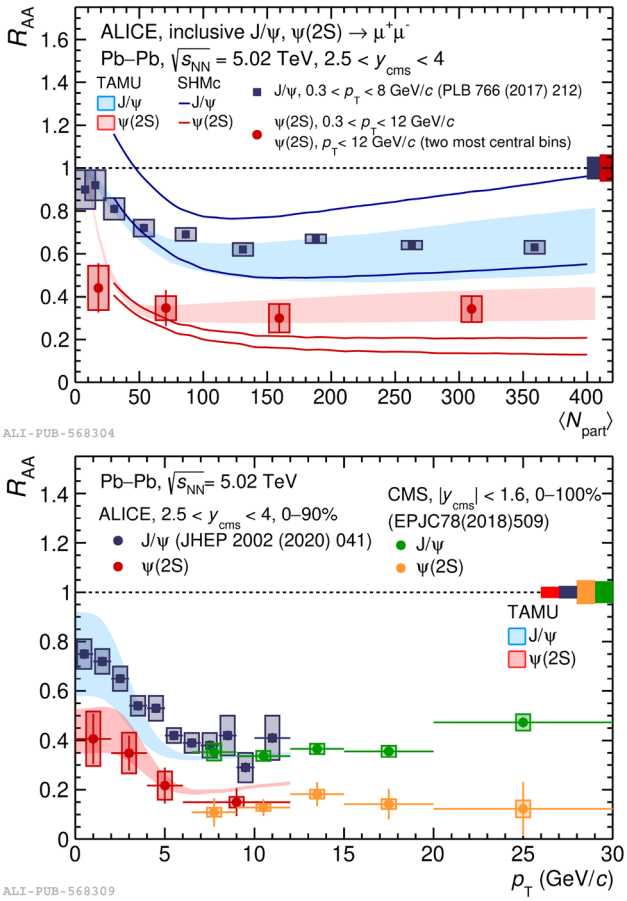

Fig. 16 (Color online) p_T-integrated (upper panel) and p_T-differential (lower panel) $\psi(2S)$ and J/ψ R_{AA} at forward rapidity in Pb–Pb collisions [95], results are compared with calculations from microscopic transport model [94] and statistical hadronization model [91]

The p_T-differential $\psi(2S)$ and J/ψ R_{AA} are compared in the lower panel of Fig. 16. The ALICE results are also compared with similar measurements from CMS, which cover the region of $|y| < 1.6$ and 6.5 GeV/c < p_T < 30 GeV/c. The CMS data agree with the ALICE measurements within uncertainties in the common p_T range. An increasing trend of R_{AA} toward low p_T for $\psi(2S)$, similar to J/ψ, is observed, hinting at a (re)generation process of charm and anticharm quarks in $\psi(2S)$ production. The strong suppression of $\psi(2S)$ R_{AA} at high p_T agrees within uncertainties with those of ALICE in the common p_T range.

The polarization of quarkonia in high-energy nuclear collisions can be significantly influenced by the unique conditions within the quark–gluon plasma (QGP). The fast-moving charges of the nuclei generate an intense magnetic field, oriented perpendicular to the reaction plane, which decreases rapidly [96]. Additionally, heavy-quark pair production occurs early in the collision process, and the subsequent evolution into bound states allows the strong magnetic field to potentially affect charmonium polarization. Another factor influencing quarkonia polarization is the orbital angular momentum of the medium [97]. These conditions suggest that both the magnetic field and the vorticity of the QGP can play crucial roles in modifying quarkonium polarization [4].

The measured polarization parameter λ_θ of the p_T-integrated (2 GeV/c < p_T < 6 GeV/c) inclusive J/ψ as a function of centrality in Pb–Pb collisions at forward rapidity ($2.5 < y < 4$) via the dimuon decay channels is shown in the upper panel of Fig. 17 [98]. Similar measurements as a function of p_T are shown in the lower panel of Fig. 17. A significant polarization is observed in central and semi-central collisions, with a 3.5σ effect observed. The p_T-dependence indicates that the deviation from zero is more pronounced at lower p_T, with the maximum deviation occurring in the (2 GeV/c < p_T < 4 GeV/c) range during semi-central (30–50%) collisions, where a 3.9σ effect is noted when considering the total uncertainties.

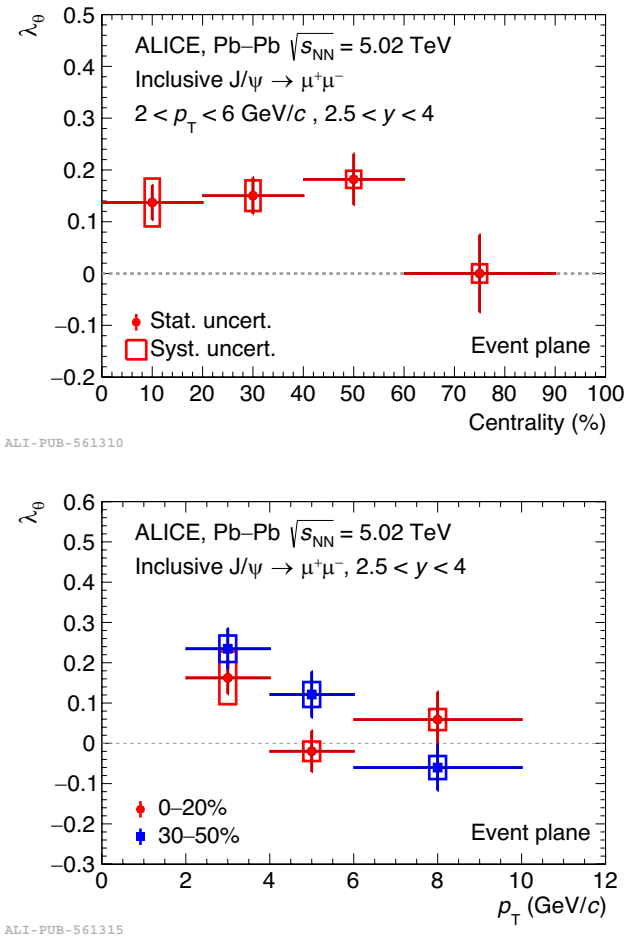

Fig. 17 (Color online) p_T-integrated (upper panel) and p_T-differential (lower panel) polarization parameters of the inclusive J/ψ λ_θ with respect to the reaction plane in Pb–Pb collisions at forward rapidity via the dimuon decay channels [98]

ALICE also measured the spin alignment of K^{*0} and ϕ mesons in Pb–Pb collisions at midrapidity [99]. The spin matrix element ρ_{00} for the polarization parameters is found to be less than 1/3 at low p_T in semi-central Pb–Pb collisions. For J/ψ mesons, the maximum λ_θ value is approximately 0.2, corresponding to a spin matrix element $\rho_{00} \approx 0.25$. Thus, the measured spin matrix elements ρ_{00} for K^{*0} and ϕ mesons in Pb–Pb collisions are all less than 1/3. Future theoretical studies on charmonium production, along with experimental improvements and increased integrated luminosity, are essential to confirm and further understand the mechanisms underlying the spin alignment of vector mesons in heavy-ion collisions.

As mentioned earlier, the magnetic field produced by the highly Lorentz-contracted ultra-relativistic heavy-ion collisions can reach magnitudes of up to 10^{15} Tesla, potentially giving rise to various exotic phenomena. The measurement of thermal dilepton production from the QGP and the hot

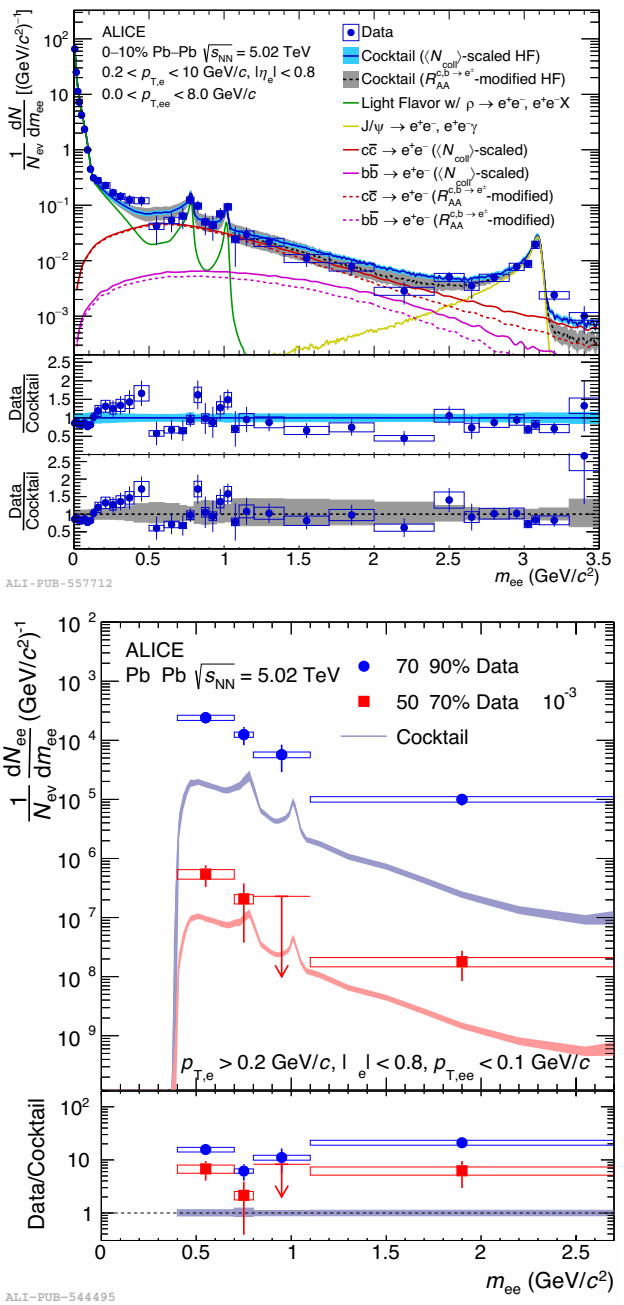

Fig. 18 (Color online) Dielectron $m_{e^+e^-}$-differential yields comparison with expected e^+e^- contributions from hadronic production decays in Pb–Pb collision at $\sqrt{s_{NN}}$ = 5.02 TeV in 0–10% centrality interval (upper panels), with similar comparisons in 50–70% and 70–90% centrality classes (lower panels) [101, 102]

hadron gas produced in heavy-ion collisions has long been recognized as a precise and powerful probe for studying the time evolution of the medium's properties [100]. The first measurement of low-mass e^+e^- pair production at low p_T in Pb–Pb collisions at $\sqrt{s_{NN}}$ = 5.02 TeV has been presented [101, 102].

The invariant mass spectra of e^+e^- pair production are shown in Fig. 18. The yield of e^+e^- pair production in the range $0.2\,\mathrm{GeV}/c < p_\mathrm{T} < 10\,\mathrm{GeV}/c$ is presented as a function of m_ee for 0–10% central Pb–Pb collisions at $\sqrt{s_\mathrm{NN}} = 5.02$ TeV (upper panel). The measurements are compared with expected contributions from known hadronic sources, specifically the $R_\mathrm{AA}^{\mathrm{c,b}\to\mathrm{e}^\pm}$-modified heavy-flavor (HF) cocktail and the N_coll-scaled HF cocktail. At low invariant masses ($0.18\,\mathrm{GeV}/c^2 < m_\mathrm{ee} < 0.5\,\mathrm{GeV}/c^2$), the ratios indicate a potential excess that is consistent with unity within certain confidence levels. Notably, this excess does not significantly depend on the method used for estimating heavy flavor. The contribution from ρ mesons, excluding medium effects, accounts for approximately 18% of the total hadronic yield; however, thermally produced e^+e^- pairs from ρ mesons are expected to be significant. In the intermediate mass range ($1.2\,\mathrm{GeV}/c^2 < m_\mathrm{ee} < 2.6\,\mathrm{GeV}/c^2$), the data are better described by the modified HF cocktail, although this region still faces considerable uncertainties. The lower panel presents the noncentral (70–90%) and semi-central (50–70%) Pb–Pb collisions at $\sqrt{s_\mathrm{NN}} = 5.02$ TeV, measured within the ALICE acceptance at midrapidity and for $p_\mathrm{T} > 0.2\,\mathrm{GeV}/c$. The yields of the produced e^+e^- pairs are compared to the expected e^+e^- production from hadronic sources, represented as "cocktails." A clear excess is observed relative to the hadronic cocktail in both centrality classes, with enhancement factors being larger in the (70–90%) collisions compared to the (50–70%) collisions. The hadronic cocktail contribution is subtracted from the inclusive e^+e^- pairs. Contributions from thermal dielectrons, arising from both the partonic and hadronic phases, are estimated using an expanding thermal fireball model that incorporates an in-medium broadened ρ spectral function [103, 104]. It is anticipated that thermal radiation from the medium will be at least an order of magnitude smaller than the measured e^+e^- pairs.

2.4 Heavy flavor probes

In ultra-relativistic heavy-ion collisions, hard scatterings involving parton constituents of nucleons can produce a variety of energetic final states, collectively referred to as "hard probes." Hard probes are energetic partons created in high momentum-transferred (high-Q^2) partonic scattering processes during the early stage of heavy-ion collisions. Since their formation time is shorter than the QGP medium's lifetime, they experience the entire medium evolution. Due to the high momentum and short-wavelength characteristics of hard probes, their interactions with the medium constituents are highly sensitive to the microscopic structure and quasi-particle nature of the medium. This makes hard probes a valuable tool for providing a "tomography" of the medium across a wide virtuality (wavelength) range. The high-Q^2 scale allows the production cross sections of hard probes to be calculated with controlled and improvable accuracy using perturbative QCD (pQCD) tools. Furthermore, the interactions between hard probes and the QGP medium can be modeled starting from the pQCD formulation of elementary collisions or transport theory, providing a firm conceptual foundation for such modeling approaches. HF quarks, jets, and photons are all examples of hard probes that have been extensively studied by ALICE during Runs 1 and 2 data collection.

For heavy quarks, such as charm and beauty quarks, the high-Q^2 scale is imparted by their large masses ($m_\mathrm{charm} \simeq 1.5\ \mathrm{GeV}/c^2$ and $m_\mathrm{beauty} \simeq 4.5\ \mathrm{GeV}/c^2$) [105], which are much larger than both Λ_QCD and the medium temperature [40]. Their production, even at low transverse momentum p_T, is predominantly governed by early stage hard partonic scatterings. The contribution from medium evolution and additional thermal production is negligible. Therefore, heavy quarks serve as self-normalized probes of the QCD medium.

When propagating through the QGP medium, heavy quarks interact with the medium constituents via both elastic (collisional) and inelastic (induced radiative) processes, leading to in-medium energy loss at low and high p_T, respectively [106, 107]. This energy loss is experimentally explored by measuring the nuclear modification factor R_AA. In the absence of QGP formation in pp collisions, $R_\mathrm{AA} = 1$ if AA collisions were simply a superposition of nucleon-nucleon collisions. However, when a heavy quark deposits most of its energy into the QGP medium, it may begin to participate in the medium's hydrodynamic expansion, potentially approaching thermalization.

The ALICE experiment measures fully reconstructed open HF hadrons from their hadronic decays at midrapidity ($|y| < 0.5$) [108–116]. In addition, open HF production is measured using semi-electronic [117–120] and semi-muonic decays [121–125] at midrapidity ($|y| < 0.8$ for low- and intermediate-p_T and $|y| < 0.6$ for high-p_T) and forward rapidity ($2.5 < y < 4$), respectively. The semi-electronic decays are also used for the partial reconstruction of charmed baryons [113, 126, 127]. Furthermore, beauty production is measured via non-prompt J/ψ from the decay mode $\mathrm{B} \to J/\psi + X$ [128–130] and non-prompt D mesons from the decay mode $\mathrm{B} \to \mathrm{D} + X$ [131, 132].

The left and right panels of Fig. 19 show, respectively, R_AA and the second-order anisotropy flow (elliptic flow) coefficient v_2 as a function of p_T for prompt D mesons measured at midrapidity in central (0–10%) and semi-central (30–50%) Pb–Pb collisions at $\sqrt{s_\mathrm{NN}} = 5.02$ TeV with ALICE [133, 134]. A significant suppression, up to a factor of five, is observed in the yields of D mesons in the

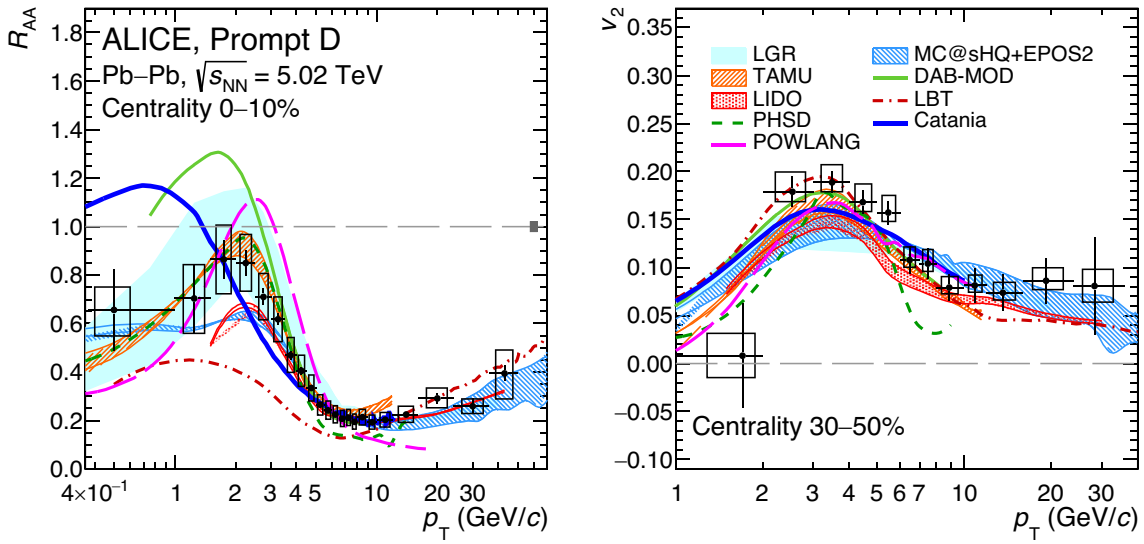

Fig. 19 (Color online) p_T-differential R_{AA} (left) and v_2 (right) of prompt D mesons measured, respectively, in 0–10% and 30–50% centrality classes at midrapidity in Pb–Pb collisions at $\sqrt{s_{NN}}$ = 5.02 TeV by ALICE [133, 134]

intermediate- and high-p_T regions in the most central 10% of Pb–Pb collisions, indicating that charm quarks undergo strong in-medium energy loss in the QGP. Furthermore, a positive v_2 of D mesons is observed at intermediate p_T in the 30–50% semi-central collisions, indicating that charm quarks participate in the collective motion of the QGP as a result of their substantial energy deposition in the medium. At low- and intermediate-p_T, i.e., $p_T \lesssim 10$ GeV/c, charm quarks exchange energy and momentum through multiple soft and incoherent collisions within the hydrodynamically expanding medium. The interaction of charm quarks with the medium is typically treated using a diffusion approach based on Fokker-Planck or Langevin dynamics, which describes their behavior in terms of Brownian motion in the QGP. Hence, the coupling between the medium and charm quarks can be expressed by the spatial diffusion coefficient D_s, which is almost independent of the quark mass and encodes the transport properties of the medium [107, 135, 136]. Furthermore, D_s is proportional to the relaxation time τ_Q of heavy particles, i.e., $\tau_Q = (m_Q/T)D_s$, where m_Q and T denote the heavy-quark mass and medium temperature, respectively.

In Fig. 19, the measurements are also compared with model calculations based on charm-quark transport in a hydrodynamically expanding QGP. All models are qualitatively in agreement with the data, including the triangular flow coefficient v_3 of D mesons [133]. Although some tension is observed, particularly at low-p_T, models that agree with data at the level $\chi^2/\mathrm{ndf} < 2$ yield a value $1.5 < 2\pi D_s T < 4.5$, where T is the temperature at the critical point of the QCD deconfinement phase transition, $T_c \simeq 155$ MeV [137, 138]. By adopting $m_{charm} = 1.5\,\mathrm{GeV}/c^2$, the corresponding charm-quark relaxation time τ_{charm} is estimated to lie in the range $3 < \tau_{charm} < 9$ fm/c. These values are similar in magnitude to the estimated lifetime of the QGP, $\tau_{QGP} \simeq 10$ fm/c at LHC energies [43], suggesting that charm quarks may fully thermalize in the QGP medium created at LHC energies.

It is worth noting that R_{AA} [121, 124] and v_2 [122] of open HF decay muons measured at forward rapidity agree with those of prompt D mesons at midrapidity within uncertainties at low- and intermediate-p_T, where the muons are primarily dominated by charm-hadron decays. This indicates that charm quarks undergo strong interactions and thermalize in the QGP medium over a wide rapidity range. The complementary measurements at forward rapidity provide significant constraints on the modeling of the longitudinal dependence of QGP transport properties [139]. In addition, the R_{AA} [124] measurements of open heavy flavors at forward rapidity have much higher precision than those at midrapidity in the high p_T, providing further constraints on the medium-induced gluon radiation behavior of beauty quarks.

To further explore the transport properties of beauty quarks in the QGP medium, non-prompt D mesons are measured at midrapidity by ALICE. The left and right panels of Fig. 20 show, respectively, the measurements of p_T-differential R_{AA} and v_2 of non-prompt D^0 mesons in central (0–10%) and semi-central (30–50%) Pb–Pb collisions at $\sqrt{s_{NN}}$ = 5.02 TeV with ALICE [132, 140]. The results are compared with the corresponding measurements of prompt D mesons [133, 134]. Similar to prompt D mesons, a significant suppression is observed in the

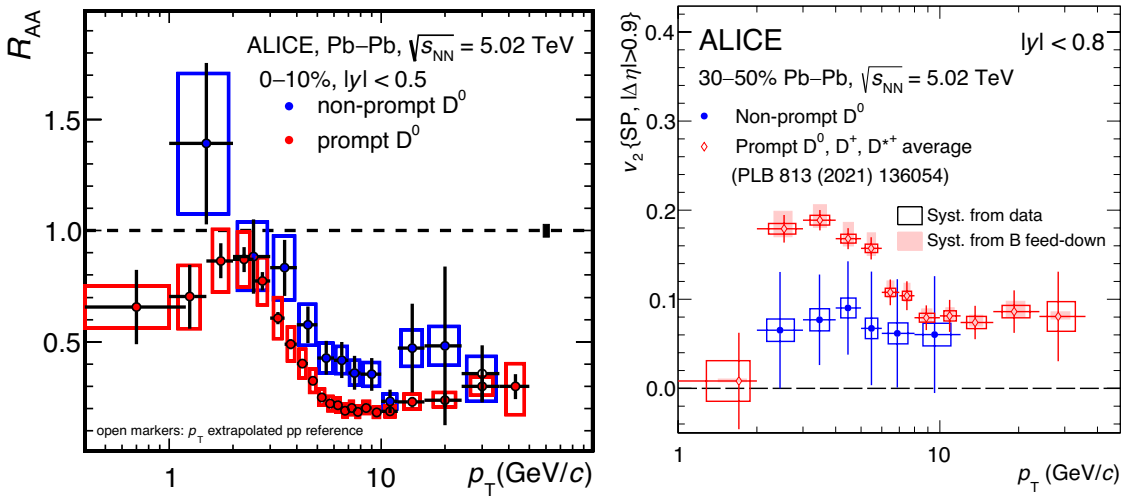

Fig. 20 (Color online) p_T-differential R_{AA} (left) and v_2 (right) of non-prompt D^0 mesons measured, respectively, in 0–10% and 30–50% centrality classes at midrapidity in Pb–Pb collisions at $\sqrt{s_{NN}}$ = 5.02 TeV by ALICE [132, 140]. Results are compared with the corresponding measurement of prompt D mesons [133, 134]

yield of non-prompt D^0 mesons at intermediate and high p_T in the most central 10% of the Pb–Pb collisions, indicating that beauty quarks also undergo substantial in-medium energy loss in the QGP. Compared to prompt D mesons, an enhancement in the non-prompt D^0-meson R_{AA} illustrates the mass-dependent in-medium energy loss of heavy quarks, resulting from the dead-cone effect [141], which causes beauty quarks to experience less energy loss in the medium relative to charm quarks.

Consistent with the large yield suppression, a positive v_2 is observed for non-prompt D^0 mesons at intermediate p_T in 30–50% semi-central collisions, with a significance of 2.7 standard deviations (σ). The measured v_2 of non-prompt D^0 mesons is lower than that of prompt D mesons, with a 3.2σ significance in the 2 GeV/c < p_T < 8 GeV/c range. Given that the spatial diffusion coefficient D_s is independent of heavy-quark mass and that m_{beauty} is approximately three times larger than m_{charm}, the beauty-quark relaxation time τ_{beauty} is likely comparable to or even longer than the QGP lifetime τ_{QGP} at the LHC. This suggests that beauty quarks are less thermalized in the QGP medium than charm quarks, leading to the observed smaller v_2 for non-prompt D^0 mesons compared to prompt D mesons at intermediate p_T. At high p_T, the measured v_2 of non-prompt D^0 mesons and prompt D mesons appears consistent, reflecting the interplay between path-length-dependent heavy-quark in-medium energy loss and the evolution and density fluctuations of the QGP medium.

The degree of thermalization of charm and beauty quarks as they interact with the QGP medium not only leads them to participate in the collective motion of the medium but also suggests their hadronization through recombination with quarks and di-quark pairs in the medium. Recombination is expected to influence the p_T distributions and the abundances of different HF hadron species in AA collisions compared to those in pp collisions [142]. Specifically, if heavy quarks hadronize via recombination, the yield of charm and beauty hadrons containing strange-quark content (e.g., D_s^+ and B_s^0 mesons) relative to non-strange hadrons is expected to be larger in AA collisions compared to pp collisions, because of the enhancement of strange-quark production in the QGP medium [143, 144]. Moreover, the production of baryons relative to mesons is expected to be enhanced at intermediate-p_T, i.e., $2 \lesssim p_T \lesssim 8$ GeV/c [145–150]. In addition, the collective radial expansion of the QGP medium, which determines a flow-velocity profile common to the thermalized particles, could also increase the baryon-to-meson yield ratio at intermediate p_T [148–150]. A precise description of the hadronization process in the hot nuclear matter is crucial to understanding the transport properties of the QGP [151].

The left panel of Fig. 21 shows the p_T-differential Λ_c^+/D^0 yield ratio measured in midrapidity in central (0–10%) and semi-central (30–50%) Pb–Pb collisions at $\sqrt{s_{NN}}$ = 5.02 TeV by ALICE. The measurements are compared with those obtained from pp collisions at the same binary center-of-mass collisions [153]. The ratios increase from pp to mid-central and central Pb–Pb collisions for 4 < p_T < 8 GeV/c, with a significance of 2.0σ and 3.7σ, respectively. This trend is qualitatively consistent with charm-quark transport in an expanding medium using the Langevin approach and hadronization primarily via coalescence in Pb–Pb collisions [149, 156]. The right panel of Fig. 21 reports the p_T-differential R_{AA} double ratio of

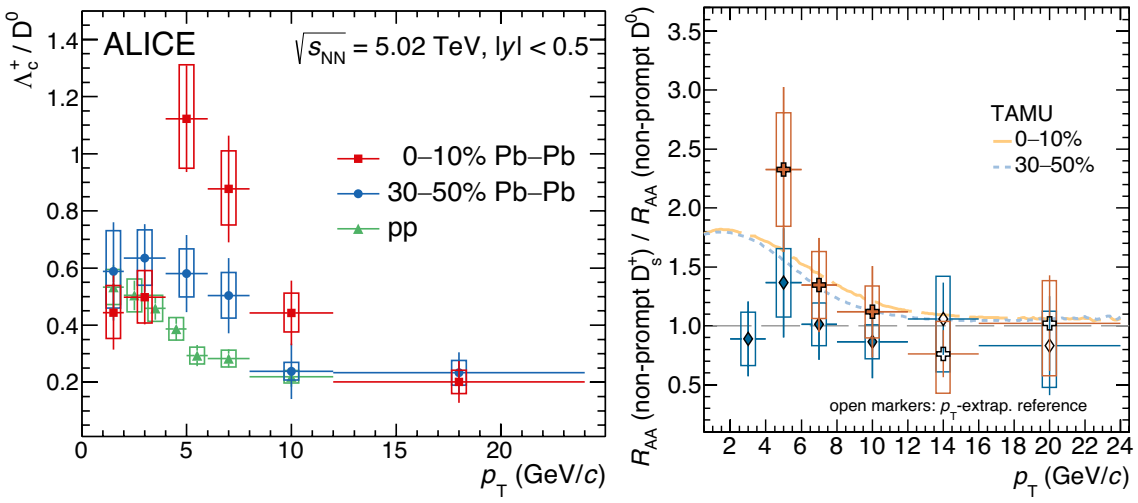

Fig. 21 (Color online) Left: Λ_c^+/D^0 ratio measured at midrapidity in central (0–10%) and semi-central (30–50%) Pb–Pb collisions at $\sqrt{s_{NN}}$ = 5.02 TeV by ALICE [152]. The measurements are compared with those obtained from pp collisions at the same binary center-of-mass energy [153]. Right: p_T-differential double ratio of R_{AA} between non-prompt D_s^+ and D^0 measured at midrapidity for 0–10% and 30–50% centrality intervals in Pb–Pb collisions at $\sqrt{s_{NN}}$ = 5.02 TeV by ALICE [154]. The measurements are compared with TAMU model predictions [155]

non-prompt D_s^+ mesons to non-prompt D^0 mesons for the 0–10% and 30–50% centrality intervals in Pb–Pb collisions at $\sqrt{s_{NN}}$ = 5.02 TeV measured by ALICE [154]. Measuring non-prompt D_s^+ mesons alongside non-prompt D^0 mesons provides the potential to shed light on the beauty-quark hadronization mechanisms in the QGP medium, as approximately 50% of non-prompt D_s^+ mesons are produced from strange-beauty meson B_s^0 decays in pp collisions [105, 131]. The double ratio measured in the most central 10% of collisions suggests a possible enhancement relative to unity in the range $4 < p_T < 12$ GeV/c. The rise at low p_T may result from an enhanced production of strange-beauty mesons compared to non-strange-beauty mesons in heavy-ion collisions. This is expected in scenarios where the abundance of strange quarks thermally produced in the QGP medium and the dominance of beauty-quark hadronization via recombination with surrounding quarks in a strangeness-enriched environment play a significant role. The TAMU model [155], which incorporates beauty-quark hadronization via recombination with light quarks from the medium, describes the data within experimental uncertainties.

An accurate interpretation of all the aforementioned measurements in heavy-ion collisions, which is crucial for characterizing the properties of the QGP medium, depends on a reference system in which the QGP medium is not formed. Traditionally, small-system collisions (e.g., pp and p–Pb), due to their dilute partonic environment, serve as the baseline for AA collision studies. In addition, measuring HF production in pp collisions provides a fundamental test for pQCD calculations in the TeV domain [157, 158].

The production cross sections of $c\bar{c}$ [159] and $b\bar{b}$ [128, 131, 160–162] at midrapidity in pp collisions have been measured by ALICE. For the $c\bar{c}$ measurements, the results are higher than the upper edge of pQCD-based FONLL and NNLO calculations, though compatible within approximately $\sim 1\sigma$ of the experimental uncertainties. The measured $b\bar{b}$ production cross sections are found to be compatible with FONLL and NNLO calculations. It is worth noting that the uncertainties in the $c\bar{c}$ measurements are significantly smaller than those in the theoretical predictions, thereby imposing stricter constraints on the theoretical calculations. Similar observations arise from the (p_T, y)-double-differential comparison of FONLL predictions with the cross sections of muons from the semi-leptonic decays of charm and beauty hadrons measured at forward rapidity [163, 164]. These measurements set additional constraints for pQCD calculations in a kinematic region important for probing parton distribution functions (PDFs) at low Bjorken-x values, down to approximately $\sim 10^{-5}$.

The mentioned theoretical calculations are based on pQCD factorization approaches [170, 171], where fragmentation functions are typically parametrized from measurements performed in e^-e^+ or ep collisions, assuming that the hadronization of heavy quarks into hadrons is a universal process across different colliding systems. However, this assumption may be violated by higher-twist effects or other factors related to heavy-quark kinematics and the underlying event in pp collisions [172–174]. This effect is observed in recent measurements of charmed meson-to-baryon

yield ratios at midrapidity in pp collisions at various collision energies for Λ_c^+/D^0 [112, 153, 175], $\Sigma_c^{0,++}/D^0$ [176], $\Xi_c^{+,0}/D^0$ [113, 126, 127], and Ω_c^0/D^0 [177]. The ALICE results reveal higher baryon-to-meson cross section ratios at low-p_T compared to e^-e^+ and ep collisions. Notably, the $\Sigma_c^{0,++}$ and $\Xi_c^{+,0}$ cross sections have been measured for the first time in hadronic collisions. A consequence of the significant difference between the charmed baryon-to-meson yield ratios measured in pp and e^-e^+ and ep collisions is that the charm-quark fragmentation fractions, $f(c \to h_c)$, i.e., the probabilities of a charm-quark hadronizing into a given charmed hadron species h_c, obtained in pp collisions differ from those estimated from e^-e^+ and ep data, as presented in the left panel of Fig. 22. In addition, $f(c \to h_c)$ is also extracted from p–Pb collisions by ALICE [178]. The results are nearly identical to those from pp collisions, indicating no significant modification of charm-quark hadronization between the two colliding systems, despite the larger system size and higher charged-particle multiplicity density in p–Pb collisions. These observations provide evidence that the assumption of universality (colliding-system independence) of parton-to-hadron fragmentation functions is not valid for charmed hadron production.

Furthermore, the measurements in p–Pb collisions are crucial for constraining cold nuclear matter (CNM) effects [179], which include nuclear modified PDFs (nPDFs), multiple scatterings in nucleons that collide with more than one other nucleon, the Cronin effect, parton energy loss in CNM, and absorption of produced hadrons by the nucleus. ALICE measures the nuclear modification factors of open HF particles in p–Pb collisions for D mesons [180], Λ_c^+ [181], and Ξ_c^0 [182] baryons, as well as open HF hadron decay electrons [118] at midrapidity and open HF decay muons [123] at forward rapidity. The measurements of open HF hadron decay muons at forward rapidity, in conjunction with the measurement of $W^{\pm}$-boson production [183] in the same rapidity region, also provide important constraints on nPDFs at Bjorken-x values down to 10^{-6}. In addition, the nuclear modification factors for beauty-quark production in p–Pb collisions have been measured by ALICE for beauty-hadron decay electrons [184] and b-tagged jets [185] at midrapidity. All these measurements are consistent with predictions that consider only the CNM effects, within both experimental and theoretical uncertainties.

Up to now, all the aforementioned observations in small-system collisions indicate that such systems can be considered as baseline references, in which the conditions to form the QGP cannot be reached. Surprisingly, as illustrated in the right panel of Fig. 22, a nonzero v_2 coefficient for open HF hadron decay muons—considered emblematic signatures of QGP formation—is observed at forward rapidity in high-multiplicity p–Pb collisions at $\sqrt{s_{NN}} = 8.16$ TeV by ALICE [167]. A similar observation is also found at midrapidity for open HF hadron decay electrons [186]. The measurements are compared with AMPT [168] and CGC [169] calculations. In the AMPT model, the anisotropy is derived from the escape mechanism via partonic interactions. On the other hand, the CGC calculations are based on the dilute-dense formalism, where interactions between partons from the proton projectile and dense gluons inside the target Pb nucleus at the early stage of the collision generate azimuthal anisotropies. For muons measured in the ALICE forward muon spectrometer, the HF contribution is the primary source for $p_T > 2$ GeV/c. Despite CGC calculations

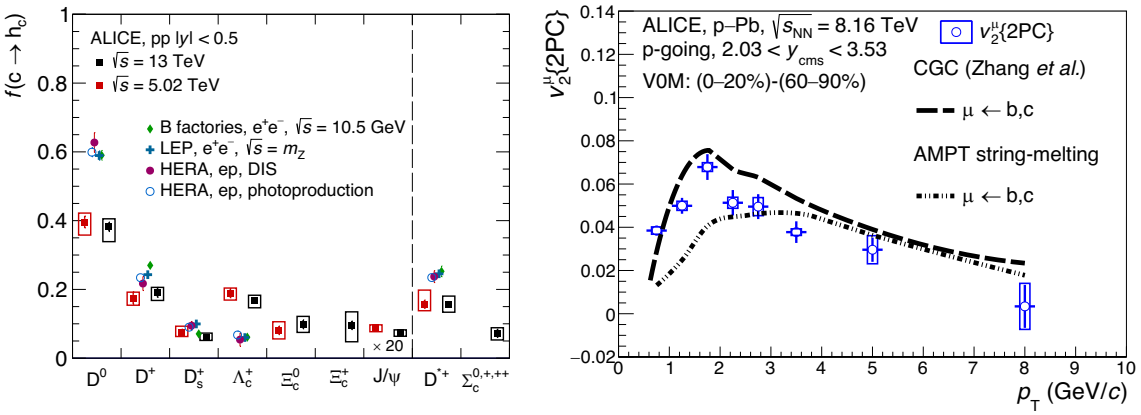

Fig. 22 (Color online) Left: charm-quark fragmentation fractions $f(c \to h_c)$ measured at midrapidity in pp collisions at $\sqrt{s} = 5.02$ TeV and 13 TeV by ALICE [165]. The results are compared with those obtained from e^-e^+ and ep collisions [166]. On the right: p_T-differential v_2 coefficient of muons, measured using the two-particle correlation (2PC) method at forward rapidity in high-multiplicity p–Pb collisions at $\sqrt{s_{NN}} = 8.16$ TeV by ALICE [167] is presented. The measurements are compared with AMPT [168] and CGC [169] calculations

overestimating the measurements in the first few data p_T intervals, the two predictions generally agree with the observed anisotropy within experimental uncertainties. The model comparison suggests that either initial- or final-state partonic interactions may generate the hydrodynamic-like azimuthal anisotropy in momentum space for HF particles. Besides, the existence of small QGP droplets at high multiplicity in small-system collisions remains a topic of debate.

In the future, the high-multiplicity LHC project for ALICE during LHC Run 3 and Run 4, along with the ALICE 3 detector upgrade project for LHC Run 5 and beyond (see Sect. 3), will be crucial for revealing the origins of the observed non-universality in charm-quark hadronization and the QGP-like effects observed in small-system collisions.

2.5 Jets

Jets play a crucial role in ultra-relativistic heavy-ion collisions, serving multiple key functions. They help identify the initial momentum scale of hard scatterings, especially for photons and other colorless probes. Moreover, jets offer valuable insights into the interactions within the dense QCD medium, particularly those involving quarks and gluons, which carry QCD color charge. By studying jet substructure, HF quarks, and the highest transverse-momentum jets, researchers can thoroughly explore interactions within the QCD medium across various topologies and kinematic ranges.

In Fig. 23, the nuclear modification factors are depicted for $R = 0.6$ (left) and the double ratio of jet nuclear modification factors between $R = 0.6$ and $R = 0.2$ (right), presented for 0–10% central Pb–Pb collisions and compared to theoretical calculations incorporating jet quenching [187]. The double ratio R_{AA} is a critical measure for evaluating the R-dependence of energy loss in jets. Values below unity indicate greater suppression for jets with larger R, values at unity suggest no R-dependence or a balancing of effects, and values above unity imply less suppression for larger R jets. In 0–10% central collisions, the $R_{AA}^{0.6/0.2}$ ratio shows suppression below unity at lower jet p_T values, indicating a potential R -dependence within the uncertainties.

Event-shape engineering (ESE) is an experimental technique that classifies events based on their anisotropies using the magnitude of the reduced flow vector, providing a novel method to constrain the path-length dependence

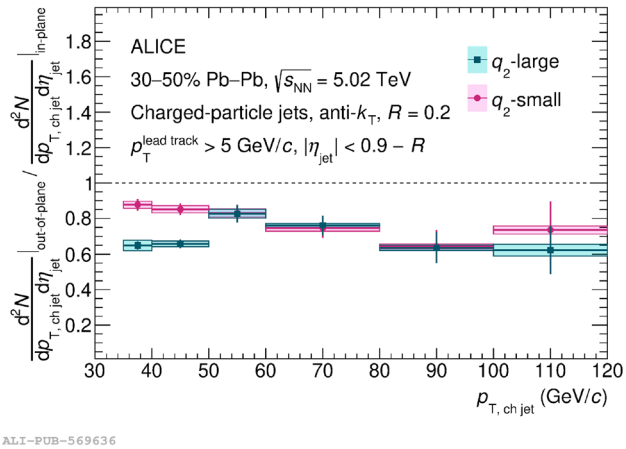

Fig. 24 (Color online) Ratios of out-of-plane to in-plane charged-particle jet yields for q_2-large and q_2-small event classes in Pb–Pb collisions at $\sqrt{s_{NN}}$ = 5.02 TeV [188]

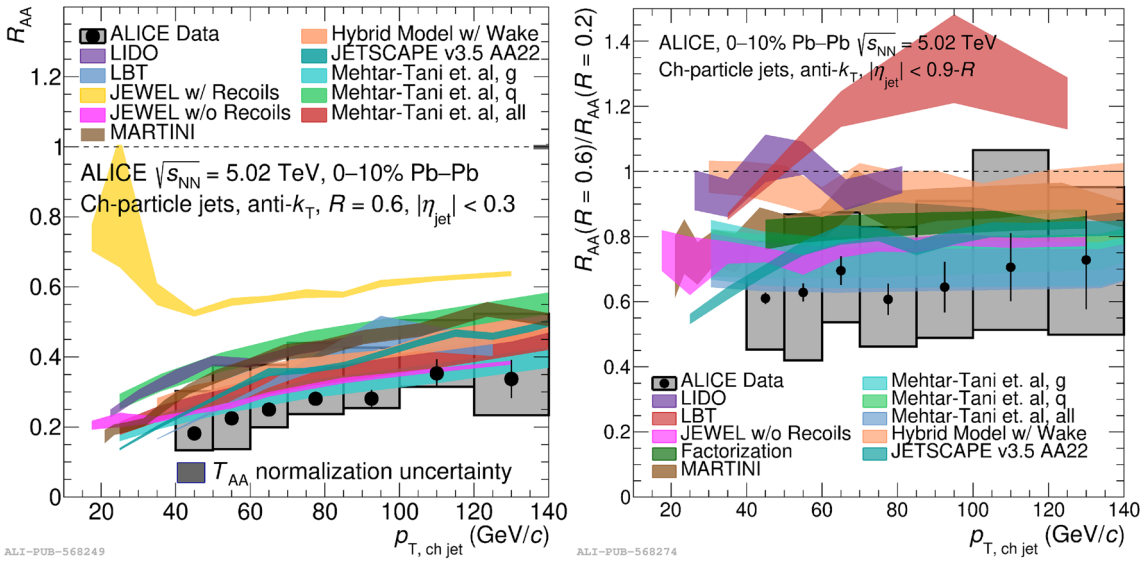

Fig. 23 (Color online) Nuclear modification factors for $R = 0.6$ (left) and double ratio of jet nuclear modification factors between $R = 0.6$ and $R = 0.2$ (right), shown at central 0–10% of Pb–Pb collisions compared to theoretical calculations incorporating jet quenching [187]

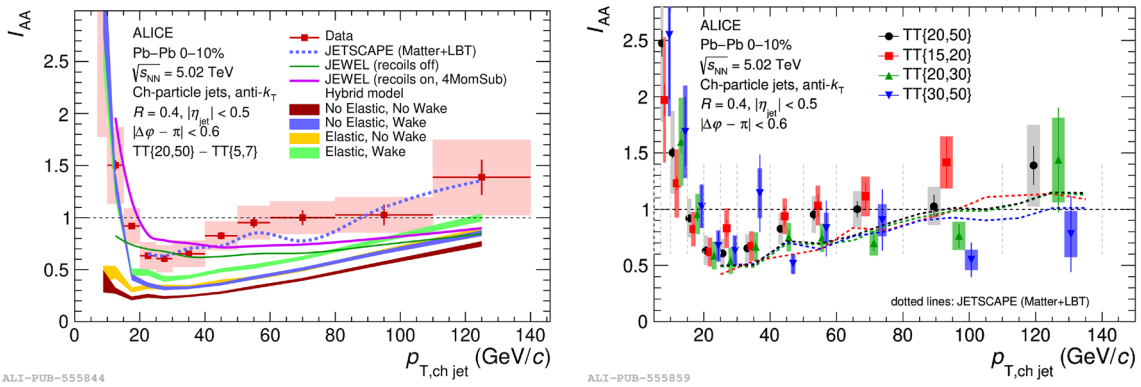

Fig. 25 (Color online) $I_{AA}(p_{T,ch\ jet})$ from $\Delta_{recoil}(p_{T,\ jet})$ distributions measured for $R = 0.4$ with default TT_{sig} selection (left) and with varied TT_{sig} selections (right) in central Pb–Pb collisions [189]

of jet energy loss. To investigate the event-shape dependence, events were categorized based on the magnitude of the reduced flow vector q_2, measured with the forward detector V0C. Figure 24 shows the ratio of out-of-plane to in-plane jet yields for the q_2-small and q_2-large event classes, focusing on jets with $R = 0.2$ in mid-central 30–50% Pb–Pb collisions at $\sqrt{s_{NN}} = 5.02$ TeV [188]. The observed ratios are significantly below unity, indicating that jets lose more energy on average when traveling out-of-plane compared to in-plane. This finding supports the notion that the extent of jet energy loss is influenced, at least partially, by the path length through the medium.

Medium-induced yield modification is measured by $I_{AA}(p_{T,ch\ jet}) = \Delta_{recoil}(\text{Pb}-\text{Pb})/\Delta_{recoil}(pp)$, which represents the ratio of the $\Delta_{recoil}(p_{T,\ jet})$ distributions measured in Pb–Pb and pp collisions. Figure 25 presents the $I_{AA}(p_{T,ch\ jet})$ distributions measured for $R = 0.4$ with the default TT_{sig} selection (left panel) and with varied TT_{sig} selections (right panel) in central Pb–Pb collisions. The $I_{AA}(p_{T,ch\ jet})$ distributions show a notable dependence on $p_{T,ch\ jet}$. For $R = 0.4$, JEWEL (recoils on) exhibits a significant increase in $I_{AA}(p_{T,ch\ jet})$ toward low $p_{T,ch\ jet}$ for $p_{T,ch\ jet} < 20$ GeV/c, mirroring the trend in the data for $R = 0.4$. Overall, JETSCAPE most accurately describes both the magnitude and $p_{T,ch\ jet}$ dependence of $I_{AA}(p_{T,ch\ jet})$ in the range $p_{T,ch\ jet} > 20$ GeV/c. The rising trend in the data toward low $p_{T,ch\ jet}$ for $p_{T,ch\ jet} < 20$GeV/c is captured by both the Hybrid Model and JEWEL, but only with the inclusion of medium-response effects [189, 190]. Figure 25 (right) displays the $I_{AA}(p_{T,ch\ jet})$distribution for $R = 0.4$ measured for several p_T^{trig} intervals used in the TT_{sig} event selection. A higher p_T^{trig} threshold corresponds to larger $\tilde{z}$, where the assumptions underlying the surface-bias picture may better apply. The results indicate that as the lower p_T^{trig} bound is raised, the rate of increase in $I_{AA}(p_{T,ch\ jet})$ at large $p_{T,ch\ jet}$ diminishes.

Figure 26 presents the first observation of medium-induced jet acoplanarity broadening in the QGP. The broadening is significant in the range of 10 GeV/$c < p_{T,ch\ jet} < 20$ GeV/c for $R = 0.4$ and 0.5, but it is negligible for $R = 0.2$, and at larger $p_{T,ch\ jet}$ for all R. This rapid transition in the shape of the acoplanarity distribution as a function of both $p_{T,ch\ jet}$ and R is striking. Possible mechanisms for generating acoplanarity broadening include jet scattering from QGP quasi-particles, medium-induced wake effects, and jet splitting, where medium-induced radiation from a high-$p_{T,ch\ jet}$

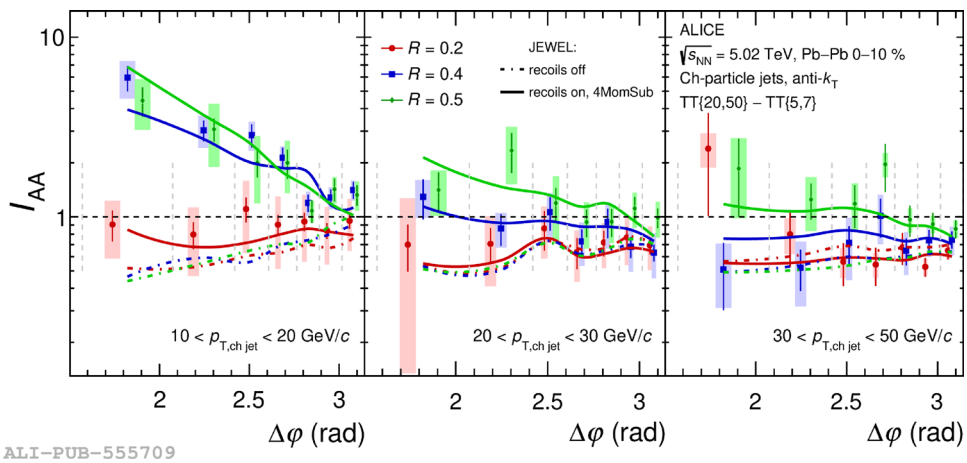

Fig. 26 (Color online) $I_{AA}(\Delta(\text{phi}))$ for $R = 0.2$, 0.4 and 0.5, for intervals in recoil $p_{T,ch\ jet}$: [10,20], [20,30], and [30,50] GeV/c. Predictions from JEWEL are also shown [190]

jet is reconstructed at low $p_{\mathrm{T,ch\ jet}}$ with a large deviation from $\Delta(\mathrm{phi}) \sim \pi$ [189, 190].

Jet quenching, a phenomenon associated with the formation of QGP in large nuclear systems, is anticipated to occur in smaller systems, albeit with diminished effects. Currently, there is no definitive evidence, beyond experimental uncertainties, of jet quenching in small systems. This raises the question of whether the observed collective effects in these systems genuinely stem from QGP formation or from other mechanisms. Further investigations are essential to search for jet quenching effects in small systems and to address this unresolved issue.

To investigate the p_{T} dependence of normalized jet production as a function of self-normalized charged-particle multiplicity, Fig. 27 displays the self-normalized jet yields across four selected jet p_{T} intervals for resolution parameters $R = 0.3$, 0.5, and 0.7. The data are also compared with PYTHIA8 predictions [191]. The measured jet production ratios in central rapidity exhibit an increase with multiplicity, mirroring earlier findings for identified particles using the forward multiplicity V0 estimator. However, the increase is less pronounced for the lowest jet p_{T} in the highest multiplicity interval. Current Monte Carlo (MC) event generators can predict the rising trend but fail to accurately describe the absolute yields, particularly in the highest multiplicity class.

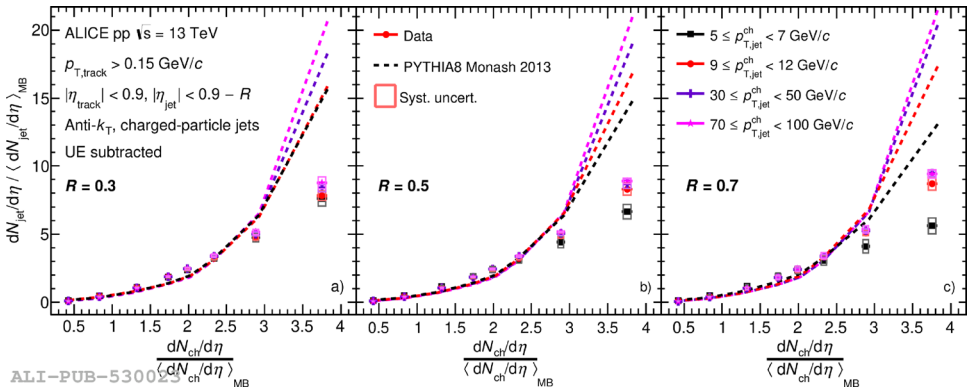

Fig. 27 (Color online) Comparison of self-normalized jet yields as a function of self-normalized charged-particle multiplicity in four selected jet p_{T} intervals (5 GeV/$c \le p_{\mathrm{T,jet}}^{\mathrm{ch}} <$ 7 GeV/c, 9 GeV/$c \le p_{\mathrm{T,jet}}^{\mathrm{ch}} <$ 12 GeV/c, 30 GeV/$c \le p_{\mathrm{T,jet}}^{\mathrm{ch}} <$ 50 GeV/c, and 70 GeV/$c \le p_{\mathrm{T,jet}}^{\mathrm{ch}} <$ 100 GeV/c) for given jet radii: a) $R = 0.3$, b) $R = 0.5$, c) $R = 0.7$ between data and PYTHIA8 predictions [191]

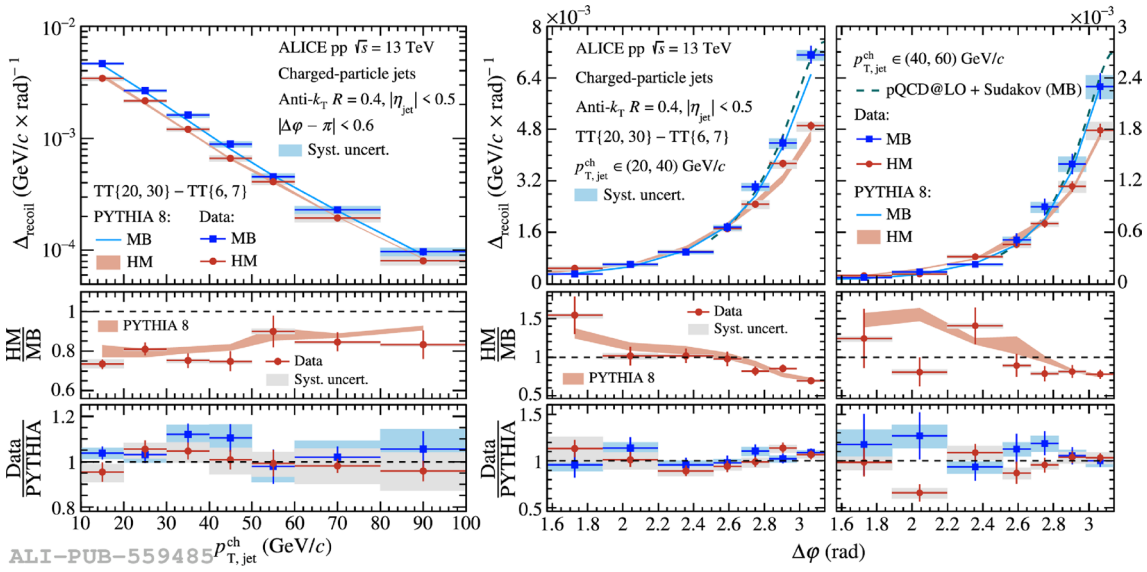

Fig. 28 (Color online) Fully corrected Δ_{recoil} distributions measured in MB and HM-selected events in pp collisions at $\sqrt{s} = 13$ TeV. Left panel: $\Delta_{\mathrm{recoil}}(p_{\mathrm{T,ch\ jet}})$ in $|\Delta(\mathrm{phi}) - \pi| < 0.6$; middle and right panels: $\Delta_{\mathrm{recoil}}(\Delta(\mathrm{phi}))$ for 20 GeV/$c < p_{\mathrm{T,ch\ jet}} <$ 40 GeV/c and 40 GeV/$c < p_{\mathrm{T,ch\ jet}} <$ 60 GeV/c [192]

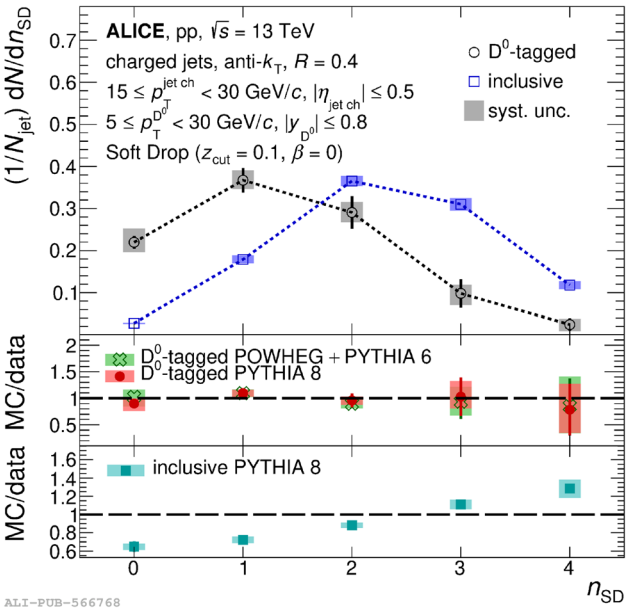

Fig. 29 (Color online) The n_{SD} distributions of prompt D^0-tagged jets compared to those of inclusive jets for 15 GeV/$c \le p_{\text{T, jet}} < 30$ GeV/c in pp collisions at $\sqrt{s} = 13$ TeV [193]

Figure 28 presents fully corrected distributions of $\Delta_{\text{recoil}}(p_{\text{T,ch jet}})$ and $\Delta_{\text{recoil}}(\Delta(\text{phi}))$ measured in minimum bias (MB) and high multiplicity (HM)-selected pp collisions at $\sqrt{s} =$ 13 TeV, alongside calculations from various models [192]. The comparison of MB and HM $\Delta_{\text{recoil}}(p_{\text{T,ch jet}})$ distributions shows a yield suppression in HM collisions that remains largely independent of $p_{\text{T, jet}}$, although there is a slight indication of a harder recoil jet spectrum for HM events. The $\Delta_{\text{recoil}}(\Delta(\text{phi}))$ distributions reveal that jet yield suppression in HM events primarily occurs in the back-to-back configuration. While the total yield is reduced, the azimuthal distribution is broadened. This broadening may result from jet quenching, where medium-induced jet scattering is more prevalent in HM events. However, PYTHIA 8 particle-level distributions also show jet yield suppression and azimuthal broadening in HM-selected events, accurately matching the measured distributions. Since PYTHIA 8 does not account for jet quenching, this suggests that jet quenching is not the dominant factor causing the observed broadening in the data.

Moreover, the count of emissions produced by the charm quark that meet the soft drop criterion, represented as n_{SD}, is determined by examining all branch splittings involving the D^0 meson. This analysis reveals a significant correlation with the number of perturbative emissions originating directly from the charm quark.

The initial measurement, correlating with the charm-quark splitting function, is depicted through the n_{SD} distribution illustrated in Fig. 29. This distribution pertains to charm jets identified by a prompt D^0 meson within the transverse momentum range 15 GeV/$c \le p_{\text{T, jet}} < 30$ GeV/c [193]. Compared to inclusive jets, the n_{SD} distribution for charm-tagged jets exhibits a noticeable shift toward smaller values. This observation suggests that, on average, charm quarks emit fewer gluons with sufficiently high p_{T} to satisfy the soft drop condition during the showering process, in contrast to light and massless partons. This behavior aligns with expectations arising from the presence of a "dead cone" effect specific to charm quarks, which leads to a steeper fragmentation pattern for charm quarks relative to light quarks and gluons.

The observable utilized to detect the dead cone involves forming the ratio of the splitting angle (θ) distributions between jets tagged with D^0-mesons and inclusive jets, grouped into bins of E_{Radiator}. Expressing this ratio in terms of the logarithm of the inverse of the angle is appropriate, as at leading order, the QCD likelihood for a parton to split is proportional to $\ln(1/\theta)\ln(k_{\text{T}})$.

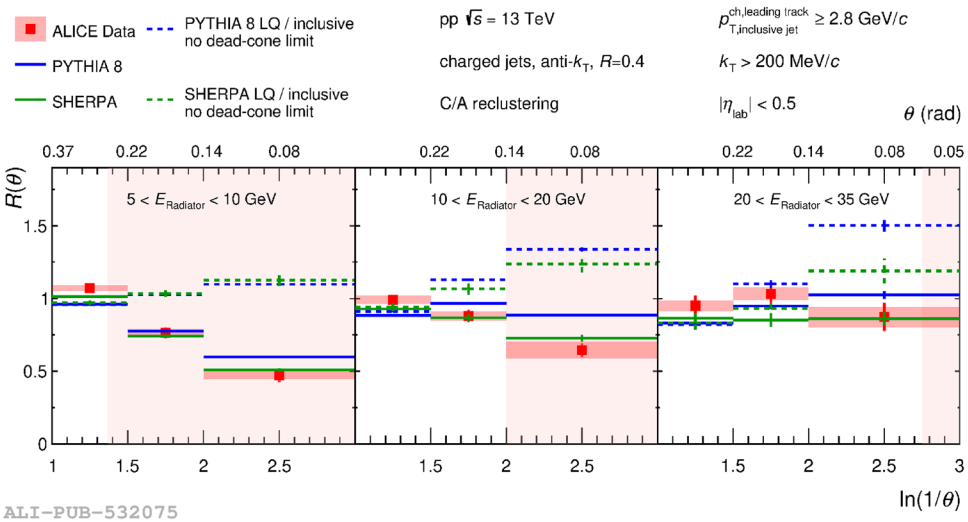

Fig. 30 (Color online) Nuclear modification factors for $R = 0.6$ (left) and double ratio of jet nuclear modification factors between $R = 0.6$ and $R = 0.2$ (right), shown for central 0–10% of Pb–Pb collisions compared to theoretical calculations incorporating jet quenching [194]

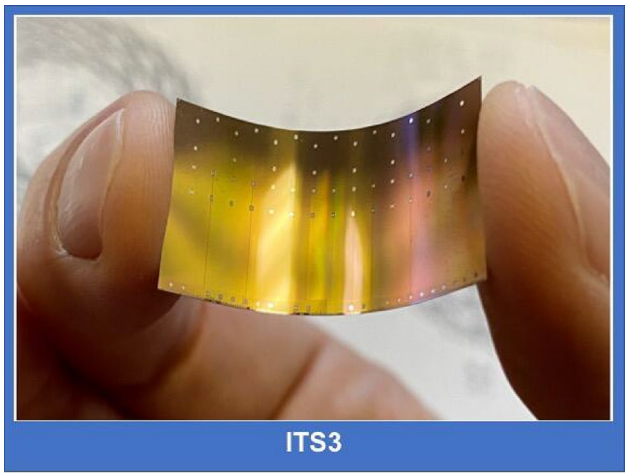

Fig. 31 (Color online) New bent wafer-scale ultra-thin monolithic pixel detector ITS3 is planned to be installed during LHC LS3

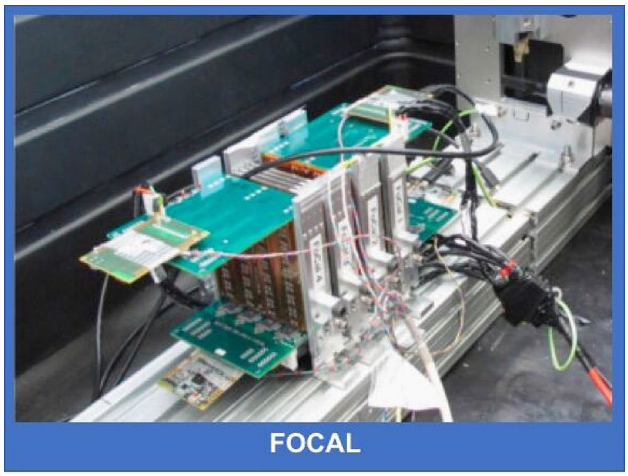

Fig. 32 (Color online) FoCal is a highly granular electromagnetic calorimeter combined with conventional sampling hadronic calorimeter covering forward pseudorapidities

Figure 30 presents measurements of $R(\theta)$ in three intervals of radiator energy associated with charm quarks: $5\,\text{GeV} < E_{\text{Radiator}} < 10\,\text{GeV}$, $10\,\text{GeV} < E_{\text{Radiator}} < 20\,\text{GeV}$, and $20\,\text{GeV} < E_{\text{Radiator}} < 35\,\text{GeV}$ [194]. A pronounced reduction in the occurrence of small-angle splittings is evident in jets tagged with D^0 mesons compared to the general jet sample. Each plot includes a baseline corresponding to scenarios without a dead cone for every MC generator (dashed lines). The discrepancy between the measured data points and the no dead-cone limit directly illustrates the presence of a dead cone, where emissions from charm quarks are suppressed. This suppression becomes more pronounced with lower radiator energies, consistent with the anticipated inverse relationship between the dead-cone angle and radiator energy.

3 ALICE detector upgrade and future plan

Two detector upgrades for ALICE have recently been approved for Run 4, to be installed during the Long Shutdown 3 of the LHC, in order to further enhance the physics reach of the experiment. The first upgrade involves enhancing the innermost three layers of the ITS (ITS3) [195]. The second upgrade entails the construction of a new forward calorimeter (FoCal) [196], optimized for direct photon detection in the forward direction of the ALICE detector.

The current upgraded ITS2 is the largest pixel detector to date, with $10\,\text{m}^2$ of active silicon area and approximately 12.5 billion pixels. In the new ITS3 (Fig. 31), the three innermost layers will be replaced with ultra-thin wafer-scale silicon sensors measuring up to $10\,\text{cm} \times 26\,\text{cm}$, built using a novel stitching technology. The sensors will be thinned to about 50 µm and bent into truly cylindrical detector layers, which are held in place with carbon foam and cooled by forced airflow. No further mechanical support or electrical connections (circuit boards) are necessary within the active area, resulting in a material budget of $0.07\%\text{X}_0$ per layer. These true cylinders will also allow the innermost layer to be positioned closer to the interaction point at 19 mm, which is only 2 mm away from the beam pipe.

Due to the reduction of the material budget and its proximity to the interaction point, the ITS3 detector will provide unprecedented spatial resolution, improved by a factor of 2 compared to that of the ITS2, as well as a higher reconstruction efficiency for low-momentum particle tracks. These features will significantly improve the physics performance of the ALICE detector for measurements of HF hadrons through the reconstruction of their decay topologies and those of dileptons.

The gain in performance [197] will enable the first measurements of B_s^0 and Λ_b^0 at low transverse momenta, as well as non-prompt D_s^+ and Ξ_c^+ decays in heavy-ion collisions at LHC energies. The initial study on the existence of the exotic ccc-deuteron may be within reach, and the precision of hypernuclei studies will also improve. In addition, the upgrade will significantly reduce the background of electrons from photon conversions in the material and semi-leptonic charm-hadron decays in the study of low-mass dielectrons. Precise measurements of these observables will provide crucial information about the properties of the quark–gluon plasma formed in heavy-ion collisions.

The FoCal detector consists of an electromagnetic calorimeter (FoCal-E) and a hadronic calorimeter (FoCal-H), covering a pseudorapidity range of $3.2 < \eta < 5.8$, as shown in Fig. 32. FoCal-E is a highly granular Si+W calorimeter composed of 18 layers of silicon pad sensors, each as small

as 1 cm × 1 cm, along with two additional silicon pixel layers featuring a pixel size of 30 µm × 30 µm. FoCal-H is constructed from copper capillary tubes and scintillating fibers.

FoCal has unique capabilities [198] to measure direct photon production at forward rapidity, allowing for probing the gluon distribution in protons and nuclei at small-x. Furthermore, FoCal will facilitate inclusive and correlation measurements of photons, neutral mesons, and jets in hadronic pp and p–Pb collisions, as well as J/ψ production in ultra-peripheral p–Pb and Pb–Pb collisions. This significantly enhances the scope of the ALICE physics program to explore the dynamics of hadronic matter and the nature of QCD evolution at small x, down to $x \sim 10^{-6}$.

The ITS3 and FoCal projects have reached the important milestone of completing their technical design reports [199, 200], which were endorsed by the CERN review committees in March 2024. The construction phase for ITS3 and FoCal has now begun, with the detectors scheduled to be installed in early 2028 and ready for data taking in 2029. A completely new detector, named 'ALICE 3', is proposed [201] for LHC Runs 5 and 6 to enable new measurements in the HF sector. This includes studies of multi-charm baryon production and the interaction potentials between heavy mesons via femtoscopy, as well as precise multi-differential measurements of di-electron emission to probe the chiral-symmetry restoration mechanism and to study the time evolution of the QGP temperature.

The ALICE 3 detector consists of a tracking system with unique pointing resolution over a large pseudorapidity range ($-4 < \eta < 4$), complemented by multiple sub-detector systems for particle identification. These include silicon TOF layers with approximately 20 ps resolution, a ring-imaging Cherenkov detector with high-resolution readout, a muon identification system, and an electromagnetic calorimeter. To achieve an unprecedented pointing resolution at midrapidity in both the transverse and longitudinal directions, the innermost layers are constructed from wafer-scale ultra-thin silicon sensors, bent into cylinders with minimal supporting material, similar to the ITS3. These layers will be positioned inside the beam pipe as close as possible to the interaction point, mounted on a retractable structure to allow sufficient aperture for the beams at injection energy. In the proposed apparatus, which includes a solenoid magnetic field of $B = 2$ T, the tracker with barrel and endcap silicon pixel layers provides a relative momentum resolution of 1–2% over a large acceptance by measuring approximately 10 space points. Intensive R&D programs are being pursued by the ALICE collaboration to push the current technological limits of silicon sensors for tracking, timing, and photon detection.

The proposed ALICE 3 detector is designed for studies of pp, p-A, and A–A collisions at luminosities that are 20–50 times higher than those achievable with the currently upgraded ALICE detector. This enhanced capability will enable a rich physics program, ranging from measurements with electromagnetic probes at ultra-low transverse momenta to precision physics in the charm and beauty sectors.

4 Summary

Since the commencement of LHC collisions in 2009, the ALICE detector has executed a highly successful data collection program. The experiment was specifically designed to investigate QCD at the LHC, utilizing the highest collision energies achievable in laboratory settings. The primary objective was to probe many-body QCD interactions at extreme temperatures by studying the formation of the QGP in heavy-ion collisions. ALICE measurements indicated that heavy-ion collisions at the LHC created conditions that far exceeded those required for the formation of the QGP. The QGP formed at LHC energies was demonstrated to undergo the most rapid expansion ever observed for a many-body system in the laboratory. ALICE also provided an extensive mapping of hadro-chemistry in heavy-ion collisions at LHC energies, observed the energy loss of energetic partons in the presence of the QGP and the modification of their showers, revealed significant modifications in quarkonium binding within the QGP, and discovered QGP-like signatures in high-multiplicity small-system collisions. These observations underscored the substantial progress made during the period of LHC data collection. This progress was achieved through collaborative efforts with other LHC experiments, alongside advancements in luminosity and center-of-mass energy coverage within the RHIC program. Looking forward, with the help of enhanced detector capabilities and increased luminosity at the LHC, ALICE is poised to unravel further mysteries of strong interactions and the properties of QCD matter in extreme conditions.

Acknowledgements We are grateful to the ALICE collaboration at LHC. *Postscript*: This review is dedicated to Professor Wenqing Shen on the occasion of his 80th birthday. Elected as an academician of the Chinese Academy of Sciences in 1999, Prof. Shen has held numerous academic leadership roles, including President of the Shanghai Branch of the Chinese Academy of Sciences, Deputy Director of the National Natural Science Foundation of China, and Chairman of the Shanghai Association of Science and Technology. Under his leadership, the Chinese nuclear physics community has expanded from traditional low-energy nuclear physics to high-energy nuclear physics, including activities in ALICE. In the two decades since 2000, the Chinese high-energy nuclear physics group has grown into one of the most vibrant international communities, achieving significant breakthroughs in the study of QCD matter, some of which are highlighted in this article. We also reflect on the importance of international collaborations in bringing together individuals from diverse cultural backgrounds and how teamwork can accomplish scientific objectives beyond the capabilities of individuals working alone, a principle that Prof. Shen has consistently advocated. We hold great admiration for Prof. Shen's outstanding leadership, far-sightedness, and substantial impact on the next generations of Chinese nuclear physicists.

References

1. F. Wilczek, Quantum field theory. Rev. Mod. Phys. **71**, S85–S95 (1999). https://doi.org/10.1103/RevModPhys.71.S85
2. D.J. Gross, F. Wilczek, Ultraviolet behavior of non-abelian gauge theories. Phys. Rev. Lett. **30**, 1343–1346 (1973). https://doi.org/10.1103/PhysRevLett.30.1343
3. H.D. Politzer, Reliable perturbative results for strong interactions? Phys. Rev. Lett. **30**, 1346–1349 (1973). https://doi.org/10.1103/PhysRevLett.30.1346
4. Z.T. Liang, X.N. Wang, Globally polarized quark-gluon plasma in non-central A+A collisions. Phys. Rev. Lett. **94**, 102301 (2005). [Erratum: Phys.Rev.Lett. 96, 039901 (2006)]. arXiv:nucl-th/0410079, https://doi.org/10.1103/PhysRevLett.94.102301
5. L. Adamczyk et al., Global Λ hyperon polarization in nuclear collisions: evidence for the most vortical fluid. Nature **548**, 62–65 (2017). https://doi.org/10.1038/nature23004. arXiv:1701.06657
6. M.S. Abdallah et al., Pattern of global spin alignment of ϕ and K^{*0} mesons in heavy-ion collisions. Nature **614**, 244–248 (2023). https://doi.org/10.1038/s41586-022-05557-5. arXiv:2204.02302
7. J.H. Chen, Z.T. Liang, Y.G. Ma et al., Global spin alignment of vector mesons and strong force fields in heavy-ion collisions. Sci. Bull. **68**, 874–877 (2023). https://doi.org/10.1016/j.scib.2023.04.001. arXiv:2305.09114
8. X.F. Luo, N. Xu, Search for the QCD critical point with fluctuations of conserved quantities in relativistic heavy-ion collisions at RHIC: An overview. Nucl. Sci. Tech. **28**, 112 (2017). https://doi.org/10.1007/s41365-017-0257-0. arXiv:1701.02105
9. X.G. Deng, D.Q. Fang, Y.G. Ma, Shear viscosity of nucleonic matter. Prog. Part. Nucl. Phys. **136**, 104095 (2024). https://doi.org/10.1016/j.ppnp.2023.104095
10. W. He, Y. Ma, L. Pang et al., High-energy nuclear physics meets machine learning. Nucl. Sci. Tech. **34**, 88 (2023). https://doi.org/10.1007/s41365-023-01233-z
11. Y.G. Ma, L.G. Pang, R. Wang et al., Phase transition study meets machine learning. Chin. Phys. Lett. **40**, 122101 (2023). https://doi.org/10.1088/0256-307X/40/12/122101
12. K.J. Sun, R. Wang, C.M. Ko et al., Unveiling the dynamics of little-bang nucleosynthesis. Nat. Commun. **15**, 1074 (2024). https://doi.org/10.1038/s41467-024-45474-x
13. J.H. Chen, X. Dong, X.H. He et al., Properties of the QCD matter: an experimental review of selected results from RHIC BES program. Nucl. Sci. Tech. **35** (2024). arXiv:2407.02935 https://doi.org/10.1007/s41365-024-01591-2
14. K. Aamodt, A.A. Quintana, R. Achenbach et al., The ALICE experiment at the CERN LHC. J. Instrum. **3**, S08002 (2008). https://doi.org/10.1088/1748-0221/3/08/S08002
15. S. Acharya, D. Adamová, A. Adler et al., The ALICE experiment: a journey through QCD. Eur. Phys. J. C **84**, 813 (2024). https://doi.org/10.1140/epjc/s10052-024-12935-y
16. J. Adam et al., Centrality dependence of the charged-particle multiplicity density at midrapidity in Pb-Pb collisions at $\sqrt{s_{\rm NN}}$ = 5.02TeV. Phys. Rev. Lett. **116**, 222302 (2016). https://doi.org/10.1103/PhysRevLett.116.222302
17. B. Alver et al., Charged-particle multiplicity and pseudorapidity distributions measured with the phobos detector in Au + Au, Cu + Cu, **d** + Au, and **p** + **p** collisions at ultrarelativistic energies. Phys. Rev. C **83**, 024913 (2011). https://doi.org/10.1103/PhysRevC.83.024913
18. C. Bierlich, G. Gustafson, L. Lönnblad, Diffractive and non-diffractive wounded nucleons and final states in pa collisions. J. High Energy Phys. **2016**, 139 (2016). https://doi.org/10.1007/JHEP10(2016)139
19. Y. Zhang, D. Zhang, X. Luo, Experimental study of the QCD phase diagram in relativistic heavy-ion collisions. Nucl. Tech. (in Chinese) **46**, 040001 (2023). https://doi.org/10.11889/j.0253-3219.2023.hjs.46.040001
20. S. Wu, H. Song, Critical dynamical fluctuations near the QCD critical point. Nucl. Tech. (in Chinese) **46**, 040004 (2023). https://doi.org/10.11889/j.0253-3219.2023.hjs.46.040004
21. K. Xu, M. Huang, QCD critical end point and baryon number fluctuation. Nucl. Tech. (in Chinese)**46**, 040005 (2023). https://doi.org/10.11889/j.0253-3219.2023.hjs.46.040005
22. Y. Wu, X. Li, L. Chen, Several problems in determining the QCD phase boundary by relativistic heavy ion collisions. Nucl. Tech. (in Chinese) **46**, 040006 (2023). https://doi.org/10.11889/j.0253-3219.2023.hjs.46.040006
23. Z. Zhu, Y. Zhao, D. Hou, QCD phase structure from holographic models. Nucl. Tech. (in Chinese) **46**, 040007 (2023). https://doi.org/10.11889/j.0253-3219.2023.hjs.46.040007
24. K. Sun, L. Chen, C.M. Ko, Light nuclei production and QCD phase transition in heavy-ion collisions. Nucl. Tech. (in Chinese) **46**, 040012 (2023). https://doi.org/10.11889/j.0253-3219.2023.hjs.46.040012
25. Q. Chen, G. Ma, J. Chen, Transport model study of conserved charge fluctuations and QCD phase transition in heavy-ion collisions. Nucl. Tech. (in Chinese) **46**, 040013 (2023). https://doi.org/10.11889/j.0253-3219.2023.hjs.46.040013
26. C.M. Ko, Searching for QCD critical point with light nuclei. Nucl. Sci. Tech. **34**, 80 (2023). https://doi.org/10.1007/s41365-023-01231-1
27. J.D. Bjorken, Highly relativistic nucleus-nucleus collisions: The central rapidity region. Phys. Rev. D **27**, 140–151 (1983). https://doi.org/10.1103/PhysRevD.27.140
28. J. Adam et al., Centrality dependence of the pseudorapidity density distribution for charged particles in Pb-Pb collisions at $\sqrt{s_{\rm NN}}$ = 5.02 TeV. Phys. Lett. B **772**, 567–577 (2017). https://doi.org/10.1016/j.physletb.2017.07.017. arXiv:1612.08966
29. E. Abbas et al., Centrality dependence of the pseudorapidity density distribution for charged particles in Pb-Pb collisions at $\sqrt{s_{\rm NN}}$ = 2.76 TeV. Phys. Lett. B **726**, 610–622 (2013)
30. ALICE Collaboration, System-size dependence of the charged-particle pseudorapidity density at $\sqrt{s_{\rm NN}}$ = 5.02 TeV for pp, p-Pb, and Pb-Pb collisions. arXiv:2204.10210
31. C. Loizides, J. Nagle, P. Steinberg, Improved version of the PHOBOS Glauber Monte Carlo. SoftwareX **1–2**, 13–18 (2015). https://doi.org/10.1016/j.softx.2015.05.001. arXiv:1408.2549
32. P. Braun-Munzinger, K. Redlich, J. Stachel, *Particle production in heavy ion collisions*, (WORLD SCIENTIFIC, 2004), p. 491-599. https://doi.org/10.1142/9789812795533_0008

33. E. Schnedermann, J. Sollfrank, U. Heinz, Thermal phenomenology of hadrons from 200A GeV S+S collisions. Phys. Rev. C **48**, 2462–2475 (1993). https://doi.org/10.1103/PhysRevC.48.2462
34. ALICE Collaboration, Measurement of (anti)alpha production in central Pb-Pb collisions at $\sqrt{s_{\rm NN}}$ = 5.02 TeV. (2023). arXiv:2311.11758
35. ALICE Collaboration, Measurement of $^{3}_{\Lambda}$H production in Pb-Pb collisions at $\sqrt{s_{\rm NN}}$ = 5.02 TeV. (2024). arXiv:2405.19839
36. J.H. Chen, X. Dong, Y.G. Ma et al., Measurements of the lightest hypernucleus: progress and perspective. Science Bulletin **68**, 3252–3260 (2023). https://doi.org/10.1016/j.scib.2023.11.045
37. S. Acharya et al., Production of charged pions, kaons, and (anti-) protons in Pb-Pb and inelastic pp collisions at $\sqrt{s_{\rm NN}}$ = 5.02 TeV. Phys. Rev. C **101**, 044907 (2020). https://doi.org/10.1103/PhysRevC.101.044907. arXiv:1910.07678
38. S. Acharya et al., Light (anti)nuclei production in Pb–Pb collisions at $\sqrt{s_{\rm NN}}$ = 5.02 TeV. Phys. Rev. C **107**, 064904 (2023). https://doi.org/10.1103/PhysRevC.107.064904. arXiv:2211.14015
39. T. Matsui, H. Satz, J/ψ suppression by quark-gluon plasma formation. Phys. Lett. B **178**, 416–422 (1986). https://doi.org/10.1016/0370-2693(86)91404-8
40. J. Adam et al., Direct photon production in Pb-Pb collisions at $\sqrt{s_{\rm NN}}$ = 2.76 TeV. Phys. Lett. B **754**, 235–248 (2016). https://doi.org/10.1016/j.physletb.2016.01.020. arXiv:1509.07324
41. S.S. Adler et al., Centrality dependence of direct photon production in $\sqrt{s_{\rm NN}}$ = 200GeV Au+Au collisions. Physical Review Letters **94**, 232301 (2005). https://doi.org/10.1103/physrevlett.94.232301
42. A. Adare et al., Enhanced production of direct photons in Au+Au collisions at $\sqrt{s_{\rm NN}}$ = 200 GeV and implications for the initial temperature. Phys. Rev. Lett. **104**, 132301 (2010). https://doi.org/10.1103/PhysRevLett.104.132301. arXiv:0804.4168
43. K. Aamodt et al., Two-pion Bose-Einstein correlations in central Pb-Pb collisions at $\sqrt{s_{\rm NN}}$ = 2.76 TeV. Phys. Lett. B **696**, 328–337 (2011). https://doi.org/10.1016/j.physletb.2010.12.053. arXiv:1012.4035
44. J. Adam et al., Centrality dependence of pion freeze-out radii in Pb-Pb collisions at $\sqrt{s_{\rm NN}}$ = 2.76 TeV. Phys. Rev. C **93**, 024905 (2016). https://doi.org/10.1103/PhysRevC.93.024905. arXiv:1507.06842
45. H. van Hees, C. Gale, R. Rapp, Thermal photons and collective flow at the relativistic heavy-ion collider. Phys. Rev. C **84**, 054906 (2011). https://doi.org/10.1103/PhysRevC.84.054906. arXiv:1108.2131
46. J.F. Paquet, C. Shen, G.S. Denicol et al., Production of photons in relativistic heavy-ion collisions. Phys. Rev. C **93**, 044906 (2016). https://doi.org/10.1103/PhysRevC.93.044906. arXiv:1509.06738
47. P. Aurenche, J.P. Guillet, E. Pilon et al., Recent critical study of photon production in hadronic collisions. Phys. Rev. D **73**, 094007 (2006). https://doi.org/10.1103/physrevd.73.094007
48. R. Hanbury Brown, R.Q. Twiss, A New type of interferometer for use in radio astronomy. Phil. Mag. Ser. **7**(45), 663–682 (1954). https://doi.org/10.1080/14786440708520475
49. R. Hanbury Brown, R.Q. Twiss, A Test of a new type of stellar interferometer on Sirius. Nature **178**, 1046–1048 (1956). https://doi.org/10.1038/1781046a0
50. S. Akkelin, Y. Sinyukov, The HBT interferometry of expanding sources. Phys. Lett. B **356**, 525–530 (1995). https://doi.org/10.1016/0370-2693(95)00765-D
51. S. Acharya et al., Investigations of anisotropic flow using multiparticle azimuthal correlations in *pp*, *p*- Pb, Xe-Xe, and Pb-Pb collisions at the LHC. Phys. Rev. Lett. **123**, 142301 (2019). https://doi.org/10.1103/PhysRevLett.123.142301
52. S. Acharya et al., Anisotropic flow and flow fluctuations of identified hadrons in Pb–Pb collisions at $\sqrt{s_{\rm NN}}$ = 5.02 TeV. J. High Energy Phys. **2023**, 243 (2023). https://doi.org/10.1007/JHEP05(2023)243
53. J. Adam et al., Correlated event-by-event fluctuations of flow harmonics in Pb-Pb collisions at $\sqrt{s_{\rm NN}}$ = 2.76TeV. Phys. Rev. Lett. **117**, 182301 (2016). https://doi.org/10.1103/PhysRevLett.117.182301
54. S. Acharya et al., Multiharmonic correlations of different flow amplitudes in Pb-Pb collisions at $\sqrt{s_{\rm NN}}$ = 2.76TeV. Phys. Rev. Lett. **127**, 092302 (2021). https://doi.org/10.1103/PhysRevLett.127.092302
55. Z. Moravcova (for the ALICE Collaboration), Observation of partonic flow in small collision systems with ALICE at the LHC., talk given at QM2022 (2022) https://indico.cern.ch/event/895086/contributions/4736573
56. W. Wu (for the ALICE Collaboration), Probing partonic collectivity in pp and p–Pb collisions with ALICE., talk given at IS2023 (2023) https://indico.cern.ch/event/1043736/contributions/5363771/
57. S. Acharya et al., Emergence of long-range angular correlations in low-multiplicity proton-proton collisions. Phys. Rev. Lett. **132**, 172302 (2024). https://doi.org/10.1103/PhysRevLett.132.172302
58. S. Acharya et al., Anisotropic flow in Xe-Xe collisions at $\sqrt{s_{\rm NN}}$ =5.44 TeV. Phys. Lett. B **784**, 82–95 (2018). https://doi.org/10.1016/j.physletb.2018.06.059
59. S. Acharya et al., Characterizing the initial conditions of heavy-ion collisions at the LHC with mean transverse momentum and anisotropic flow correlations. Phys. Lett. B **834**, 137393 (2022). https://doi.org/10.1016/j.physletb.2022.137393
60. Z. Lu (for the ALICE Collaboration), Probing the nuclear structure with flow observables in ALICE., talk given at IS2023 (2023) https://indico.cern.ch/event/1043736/contributions/5363770/
61. S. Acharya et al., Probing the effects of strong electromagnetic fields with charge-dependent directed flow in Pb-Pb collisions at the LHC. Phys. Rev. Lett. **125**, 022301 (2020). https://doi.org/10.1103/PhysRevLett.125.022301
62. J. Zhao, J.H. Chen, X.G. Huang et al., Electromagnetic fields in ultra-peripheral relativistic heavy-ion collisions. Nucl. Sci. Tech. **35**, 20 (2024). https://doi.org/10.1007/s41365-024-01374-9
63. Z.F. Jiang, X.Y. Wu, H.Q. Yu et al., The direct flow of charged particles and the global polarization of hyperons in 200 AGeV Au+Au collisions at RHIC. Acta Phys. Sin. **72**, 072504 (2023). https://doi.org/10.7498/aps.72.20222391
64. H. Ding, S. Li, J. Liu, Progress on QCD properties in strong magnetic fields from lattice QCD. Nucl. Tech. (in Chinese) **46**, 040008 (2023). https://doi.org/10.11889/j.0253-3219.2023.hjs.46.040008
65. Y. Jiang, J.F. Liao, Phase transitions of strong interaction matter in vorticity fields. Nucl. Tech. (in Chinese) **46**, 040011 (2023). https://doi.org/10.11889/j.0253-3219.2023.hjs.46.040011
66. X.L. Zhao, G.L. Ma, Y.G. Ma, Electromagnetic field effects and anomalous chiral phenomena in heavy-ion collisions at intermediate and high energy. Acta Phys. Sin. **72**, 112502 (2023). https://doi.org/10.7498/aps.72.20230245
67. Q.Y. Shou, J. Zhao, H.J. Xu et al., Progress on the experimental search for the chiral magnetic effect, the chiral vortical effect, and the chiral magnetic wave. Acta Phys. Sin. **72**, 112504 (2023). https://doi.org/10.7498/aps.72.20230109
68. W.Y. Wu, Q.Y. Shou, P. Christakoglou et al., Global constraint on the magnitude of anomalous chiral effects in heavy-ion collisions. Phys. Rev. C **107**, L031902 (2023). https://doi.org/10.1103/PhysRevC.107.L031902

69. C. Wang (for the ALICE Collaboration), Search for anomalous chiral effects in heavy-ion collisions with ALICE., talk given at QM2023 (2023) https://indico.cern.ch/event/1139644/contributions/5502913/
70. S. Acharya et al., Constraining the chiral magnetic effect with charge-dependent azimuthal correlations in Pb-Pb collisions at $\sqrt{s_{\rm NN}} = 2.76$ and 5.02 TeV. J. High Energy Phys. **2020**, 160 (2020). https://doi.org/10.1007/JHEP09(2020)160
71. S. Acharya et al., Search for the chiral magnetic effect with charge-dependent azimuthal correlations in Xe-Xe collisions at $\sqrt{s_{\rm NN}} = 5.44$ TeV. Phys. Lett. B **856**, 138862 (2024). https://doi.org/10.1016/j.physletb.2024.138862
72. S. Acharya et al., Probing the chiral magnetic wave with charge-dependent flow measurements in Pb-Pb collisions at the LHC. J. High Energy Phys. **2023**, 67 (2023). https://doi.org/10.1007/JHEP12(2023)067
73. S. Acharya et al., Unveiling the strong interaction among hadrons at the LHC. Nature **588**, 232–238 (2020). https://doi.org/10.1038/s41586-020-3001-6
74. L. Fabbietti, V.M. Sarti, O.V. Doce, Study of the strong interaction among hadrons with correlations at the LHC. Annu. Rev. Nucl. Part. S. **71**, 377–402 (2021). https://doi.org/10.1146/annurev-nucl-102419-034438
75. Y.G. Ma, Hypernuclei as a laboratory to test hyperon-nucleon interactions. Nuc. Sci. Tech. **34**, 97 (2023). https://doi.org/10.1007/s41365-023-01248-6
76. S. Acharya et al., Exploring the $N\Lambda$-$N\Sigma$ coupled system with high precision correlation techniques at the LHC. Phys. Lett. B **833**, 137272 (2022). https://doi.org/10.1016/j.physletb.2022.137272
77. S. Acharya et al., Investigation of the p-σ_0 interaction via femtoscopy in pp collisions. Phys. Lett. B **805**, 135419 (2020). https://doi.org/10.1016/j.physletb.2020.135419
78. S. Acharya et al., Experimental evidence for an attractive p-ϕ interaction. Phys. Rev. Lett. **127**, 172301 (2021). https://doi.org/10.1103/PhysRevLett.127.172301
79. S. Acharya et al., Study of the Λ-Λ interaction with femtoscopy correlations in pp and p-Pb collisions at the LHC. Phys. Lett. B **797**, 134822 (2019). https://doi.org/10.1016/j.physletb.2019.134822
80. S. Acharya et al., Scattering studies with low-energy kaon-proton femtoscopy in proton-proton collisions at the lhc. Phys. Rev. Lett. **124**, 092301 (2020). https://doi.org/10.1103/PhysRevLett.124.092301
81. S. Acharya et al., First study of the two-body scattering involving charm hadrons. Phys. Rev. D **106**, 052010 (2022). https://doi.org/10.1103/PhysRevD.106.052010
82. S. Acharya, D. Adamová, G. Aglieri Rinella et al., Studying the interaction between charm and light-flavor mesons. Phys. Rev. D **110**, 032004 (2024). https://doi.org/10.1103/PhysRevD.110.032004
83. S. Acharya et al., Towards the understanding of the genuine three-body interaction for p-p-p and p-p-Λ. Eur. Phys. A **59**, 145 (2023). https://doi.org/10.1140/epja/s10050-023-00998-6
84. S. Acharya, D. Adamová, G. Aglieri Rinella et al., Exploring the strong interaction of three-body systems at the LHC. Phys. Rev. X **14**, 031051 (2024). https://doi.org/10.1103/PhysRevX.14.031051
85. J. Adam et al., J/ψ suppression at forward rapidity in Pb–Pb collisions at $\sqrt{s_{\rm NN}} = 5$ TeV. Phys. Lett. B **766**, 212–224 (2017). https://doi.org/10.1016/j.physletb.2016.12.064. arXiv:1606.08197
86. S. Acharya et al., Measurements of inclusive J/ψ production at midrapidity and forward rapidity in Pb–Pb collisions at $\sqrt{s_{\rm NN}} =$ 5.02 TeV. Phys. Lett. B **849**, 138451 (2024). https://doi.org/10.1016/j.physletb.2024.138451. arXiv:2303.13361
87. S. Acharya et al., Coherent J/ψ photoproduction at forward rapidity in ultra-peripheral Pb–Pb collisions at $\sqrt{s_{\rm NN}} = 5.02$ TeV. Phys. Lett. B **798**, 134926 (2019). https://doi.org/10.1016/j.physletb.2019.134926. arXiv:1904.06272
88. S. Acharya et al., Coherent J/ψ and ψ' photoproduction at midrapidity in ultra-peripheral Pb–Pb collisions at $\sqrt{s_{\rm NN}} = 5.02$ TeV. Eur. Phys. J. C **81**, 712 (2021). https://doi.org/10.1140/epjc/s10052-021-09437-6. arXiv:2101.04577
89. J. Adam et al., Measurement of an excess in the yield of J/ψ at very low $p_{\rm T}$ in Pb–Pb collisions at $\sqrt{s_{\rm NN}} = 2.76$ TeV. Phys. Rev. Lett. **116**, 222301 (2016). https://doi.org/10.1103/PhysRevLett.116.222301. arXiv:1509.08802
90. S. Acharya, D. Adamová, A. Adler et al., Photoproduction of low-pt J/ψ from peripheral to central Pb-Pb collisions at 5.02 TeV. Phys. Lett. B **846**, 137467 (2023). https://doi.org/10.1016/j.physletb.2022.137467
91. A. Andronic, P. Braun-Munzinger, M.K. Koehler et al., Transverse momentum distributions of charmonium states with the statistical hadronization model. Phys. Lett. B **797**, 134836 (2019). https://doi.org/10.1016/j.physletb.2019.134836. arXiv:1901.09200
92. K. Zhou, N. Xu, Z. Xu et al., Medium effects on charmonium production at ultrarelativistic energies available at the CERN Large Hadron Collider. Phys. Rev. C **89**, 054911 (2014). https://doi.org/10.1103/PhysRevC.89.054911. arXiv:1401.5845
93. B. Wu, X. Du, M. Sibila et al., $X(3872)$transport in heavy-ion collisions. Eur. Phys. J. A **57**, 122 (2021). [Erratum: Eur.Phys.J.A 57, 314 (2021)]. arXiv:2006.09945, https://doi.org/10.1140/epja/s10050-021-00623-4
94. X. Zhao, R. Rapp, Charmonium in medium: from correlators to experiment. Phys. Rev. C **82**, 064905 (2010). https://doi.org/10.1103/PhysRevC.82.064905. arXiv:1008.5328
95. S. Acharya et al., $\psi(2S)$ Suppression in Pb-Pb Collisions at the LHC. Phys. Rev. Lett. **132**, 042301 (2024). https://doi.org/10.1103/PhysRevLett.132.042301. arXiv:2210.08893
96. V. Skokov, A.Y. Illarionov, V. Toneev, Estimate of the magnetic field strength in heavy-ion collisions. Int. J. Mod. Phys. A **24**, 5925–5932 (2009). https://doi.org/10.1142/S0217751X09047570. arXiv:0907.1396
97. F. Becattini, F. Piccinini, J. Rizzo, Angular momentum conservation in heavy ion collisions at very high energy. Phys. Rev. C **77**, 024906 (2008). https://doi.org/10.1103/PhysRevC.77.024906. arXiv:0711.1253
98. S. Acharya et al., Measurement of the J/ψ polarization with respect to the event plane in Pb-Pb collisions at the LHC. Phys. Rev. Lett. **131**, 042303 (2023). https://doi.org/10.1103/PhysRevLett.131.042303. arXiv:2204.10171
99. S. Acharya et al., Evidence of spin-orbital angular momentum interactions in relativistic heavy-ion collisions. Phys. Rev. Lett. **125**, 012301 (2020). https://doi.org/10.1103/PhysRevLett.125.012301. arXiv:1910.14408
100. S. Turbide, R. Rapp, C. Gale, Hadronic production of thermal photons. Phys. Rev. C **69**, 014903 (2004). https://doi.org/10.1103/PhysRevC.69.014903. arXiv:hep-ph/0308085
101. S. Acharya et al., Dielectron production in central Pb−Pb collisions at $\sqrt{s_{\rm NN}} = 5.02$ TeV. (2023). arXiv:2308.16704
102. S. Acharya et al., Dielectron production at midrapidity at low transverse momentum in peripheral and semi-peripheral Pb-Pb collisions at $\sqrt{s_{\rm NN}} = 5.02$ TeV. JHEP **06**, 024 (2023). https://doi.org/10.1007/JHEP06(2023)024. arXiv:2204.11732
103. R. Rapp, J. Wambach, Low mass dileptons at the CERN SPS: Evidence for chiral restoration? Eur. Phys. J. A **6**, 415–420

(1999). https://doi.org/10.1007/s100500050364. arXiv:hep-ph/9907502
104. R. Rapp, Dilepton spectroscopy of QCD matter at collider energies. Adv. High Energy Phys. **2013**, 148253 (2013). https://doi.org/10.1155/2013/148253. arXiv:1304.2309
105. R.L. Workman et al., Review of particle physics. PTEP **2022**, 083C01 (2022). https://doi.org/10.1093/ptep/ptac097
106. X. Dong, Y.J. Lee, R. Rapp, Open heavy-flavor production in heavy-ion collisions. Ann. Rev. Nucl. Part. Sci. **69**, 417–445 (2019). https://doi.org/10.1146/annurev-nucl-101918-023806. arXiv:1903.07709
107. F. Prino, R. Rapp, Open heavy flavor in QCD matter and in nuclear collisions. J. Phys. G **43**, 093002 (2016). https://doi.org/10.1088/0954-3899/43/9/093002. arXiv:1603.00529
108. B. Abelev et al., Measurement of charm production at central rapidity in proton-proton collisions at $\sqrt{s} = 2.76$ TeV. JHEP **1207**, 191 (2012). https://doi.org/10.1007/JHEP07(2012)191. arXiv:1205.4007
109. B. Abelev et al., Suppression of high transverse momentum D mesons in central Pb-Pb collisions at $\sqrt{s_{\rm NN}} = 2.76$ TeV. JHEP **1209**, 112 (2012). https://doi.org/10.1007/JHEP09(2012)112. arXiv:1203.2160
110. B. Abelev et al., $\rm D_s^+$ meson production at central rapidity in proton-proton collisions at $\sqrt{s} = 7$ TeV. Phys. Lett. B **718**, 279–294 (2012). https://doi.org/10.1016/j.physletb.2012.10.049. arXiv:1208.1948
111. B.B. Abelev et al., Measurement of prompt D-meson production in p–Pb collisions at $\sqrt{s_{\rm NN}} = 5$ TeV. Phys. Rev. Lett. **113**, 232301 (2014). https://doi.org/10.1103/PhysRevLett.113.232301. arXiv:1405.3452
112. S. Acharya et al., Λ_c^+ production in pp collisions at $\sqrt{s} = 7$ TeV and in p–Pb collisions at $\sqrt{s_{\rm NN}} = 5$ TeV. JHEP **1804**, 108 (2018). https://doi.org/10.1007/JHEP04(2018)108. arXiv:1712.09581
113. S. Acharya et al., First measurement of Ξ_c^0 production in pp collisions at $\sqrt{s} = 7$ TeV. Phys. Lett. B **781**, 8–19 (2018). https://doi.org/10.1016/j.physletb.2018.03.061. arXiv:1712.04242
114. S. Acharya et al., D-meson azimuthal anisotropy in midcentral Pb–Pb collisions at $\sqrt{s_{\rm NN}} = 5$ TeV. Phys. Rev. Lett. **120**, 102301 (2018). https://doi.org/10.1103/PhysRevLett.120.102301. arXiv:1707.01005
115. S. Acharya et al., Measurement of $\rm D^0$, $\rm D^+$, $\rm D^{*+}$ and $\rm D_s^+$ production in Pb-Pb collisions at $\sqrt{s_{\rm NN}} = 5$ TeV. JHEP **1810**, 174 (2018). https://doi.org/10.1007/JHEP10(2018)174. arXiv:1804.09083
116. S. Acharya et al., Λ_c^+ production in Pb–Pb collisions at $\sqrt{s_{\rm NN}} = 5$ TeV. Phys. Lett. B **793**, 212–223 (2019). https://doi.org/10.1016/j.physletb.2019.04.046. arXiv:1809.10922
117. B. Abelev et al., Measurement of electrons from semileptonic heavy-flavour hadron decays in pp collisions at $\sqrt{s} = 7$ TeV. Phys. Rev. D **86**, 112007 (2012). https://doi.org/10.1103/PhysRevD.86.112007. arXiv:1205.5423
118. J. Adam et al., Measurement of electrons from heavy-flavour hadron decays in p–Pb collisions at $\sqrt{s_{\rm NN}} = 5$ TeV. Phys. Lett. B **754**, 81–93 (2016). https://doi.org/10.1016/j.physletb.2015.12.067. arXiv:1509.07491
119. S. Acharya et al., Measurement of electrons from semileptonic heavy-flavour hadron decays at midrapidity in pp and Pb–Pb collisions at $\sqrt{s_{\rm NN}} = 5$ TeV. Phys. Lett. B **804**, 135377 (2020). https://doi.org/10.1016/j.physletb.2020.135377. arXiv:1910.09110
120. S. Acharya et al., Elliptic Flow of Electrons from Beauty-Hadron Decays in Pb-Pb Collisions at $\sqrt{s_{\rm NN}} = 5$ TeV. Phys. Rev. Lett. **126**, 162001 (2021). https://doi.org/10.1103/PhysRevLett.126.162001. arXiv:2005.11130
121. B. Abelev et al., Production of muons from heavy flavour decays at forward rapidity in pp and Pb-Pb collisions at $\sqrt{s_{\rm NN}} = 2.76$ TeV. Phys. Rev. Lett. **109**, 112301 (2012). https://doi.org/10.1103/PhysRevLett.109.112301. arXiv:1205.6443
122. J. Adam et al., Elliptic flow of muons from heavy-flavour hadron decays at forward rapidity in Pb-Pb collisions at $\sqrt{s_{\rm NN}} = 2.76$ TeV. Phys. Lett. B **753**, 41–56 (2016). https://doi.org/10.1016/j.physletb.2015.11.059. arXiv:1507.03134
123. S. Acharya et al., Production of muons from heavy-flavour hadron decays in p–Pb collisions at $\sqrt{s_{\rm NN}} = 5$ TeV. Phys. Lett. B **770**, 459–472 (2017). https://doi.org/10.1016/j.physletb.2017.03.049. arXiv:1702.01479
124. S. Acharya et al., Production of muons from heavy-flavour hadron decays at high transverse momentum in Pb-Pb collisions at $\sqrt{s_{\rm NN}} = 5.02$ and 2.76 TeV. Phys. Lett. B **820**, 136558 (2021). https://doi.org/10.1016/j.physletb.2021.136558. arXiv:2011.05718
125. S. Acharya et al., Inclusive heavy-flavour production at central and forward rapidity in Xe-Xe collisions at $\sqrt{s_{\rm NN}} = 5.44$ TeV. Phys. Lett. B **819**, 136437 (2021). https://doi.org/10.1016/j.physletb.2021.136437
126. S. Acharya et al., Measurement of the production cross section of prompt Ξ_c^0 baryons at midrapidity in pp collisions at $\sqrt{s} = 5.02$ TeV. JHEP **2110**, 159 (2021). https://doi.org/10.1007/JHEP10(2021)159. arXiv:2105.05616
127. S. Acharya et al., Measurement of the cross sections of Ξ_c^0 and Ξ_c^+ baryons and of the branching fraction ratio $\rm BR(\Xi_c^0 \to \Xi^- e^+ \nu_e)$ / $\rm BR(\Xi_c^0 \to \Xi^- \pi^+)$ in pp collisions at 13 TeV. Phys. Rev. Lett. **127**, 272001 (2021). https://doi.org/10.1103/PhysRevLett.127.272001. arXiv:2105.05187
128. B. Abelev et al., Measurement of prompt J/ψ and beauty hadron production cross sections at mid-rapidity in pp collisions at $\sqrt{s} = 7$ TeV. JHEP **1211**, 065 (2012). https://doi.org/10.1007/JHEP11(2012)065
129. J. Adam et al., Inclusive, prompt and non-prompt J/ψ production at mid-rapidity in Pb-Pb collisions at $\sqrt{s_{\rm NN}} = 2.76$ TeV. JHEP **1507**, 051 (2015). https://doi.org/10.1007/JHEP07(2015)051. arXiv:1504.07151
130. S. Acharya et al., Prompt and non-prompt $J\psi$ production and nuclear modification at mid-rapidity in p–Pb collisions at $\sqrt{s_{\rm NN}} = 5$ TeV. Eur. Phys. J. C **78**, 466 (2018). https://doi.org/10.1140/epjc/s10052-018-5881-2. arXiv:1802.00765
131. S. Acharya et al., Measurement of beauty and charm production in pp collisions at $\sqrt{s} = 5.02$ TeV via non-prompt and prompt D mesons. JHEP **2105**, 220 (2021). https://doi.org/10.1007/JHEP05(2021)220. arXiv:2102.13601
132. S. Acharya et al., Measurement of beauty production via non-prompt $\rm D^0$ mesons in Pb–Pb collisions at $\sqrt{s_{\rm NN}} = 5$ TeV. JHEP **2212**, 126 (2022). https://doi.org/10.1007/JHEP12(2022)126. arXiv:2202.00815
133. S. Acharya et al., Transverse-momentum and event-shape dependence of D-meson flow harmonics in Pb–Pb collisions at $\sqrt{s_{\rm NN}} = 5$ TeV. Phys. Lett. B **813**, 136054 (2021). https://doi.org/10.1016/j.physletb.2020.136054. arXiv:2005.11131
134. S. Acharya et al., Prompt $\rm D^0$, $\rm D^+$, and $\rm D^{*+}$ production in Pb-Pb collisions at $\sqrt{s_{\rm NN}} = 5$ TeV. JHEP **2201**, 174 (2022). https://doi.org/10.1007/JHEP01(2022)174. arXiv:2110.09420
135. R. Rapp, H. van Hees, Heavy quarks in the quark-gluon plasma. Quark-Gluon Plasma **4**, 111–206 (2010). arXiv:0903.1096, https://doi.org/10.1142/9789814293297_0003
136. B. Svetitsky, Diffusion of charmed quarks in the quark-gluon plasma. Phys. Rev. D **37**, 2484–2491 (1988). https://doi.org/10.1103/PhysRevD.37.2484

137. A. Bazavov et al., Equation of state in (2 + 1)-flavor QCD. Phys. Rev. D **90**, 094503 (2014). https://doi.org/10.1103/PhysRevD.90.094503. arXiv:1407.6387
138. S. Borsanyi, Z. Fodor, C. Hoelbling et al., Full result for the QCD equation of state with 2 + 1 flavors. Phys. Lett. B **730**, 99–104 (2014). https://doi.org/10.1016/j.physletb.2014.01.007. arXiv:1309.5258
139. C.A.G. Prado, W.J. Xing, S. Cao et al., Longitudinal dependence of open heavy flavor R_{AA} in relativistic heavy-ion collisions. Phys. Rev. C **101**, 064907 (2020). https://doi.org/10.1103/PhysRevC.101.064907. arXiv:1911.06527
140. S. Acharya et al., Measurement of non-prompt D^0-meson elliptic flow in Pb-Pb collisions at $\sqrt{s_{NN}} = 5$ TeV. Eur. Phys. J. C **83**, 1123 (2023). https://doi.org/10.1140/epjc/s10052-023-12259-3. arXiv:2307.14084
141. M. Djordjevic, M. Djordjevic, B. Blagojevic, RHIC and LHC jet suppression in non-central collisions. Phys. Lett. B **737**, 298–302 (2014). https://doi.org/10.1016/j.physletb.2014.08.063. arXiv:1405.4250
142. M. He, R.J. Fries, R. Rapp, D_s-meson as quantitative probe of diffusion and hadronization in nuclear collisions. Phys. Rev. Lett. **110**, 112301 (2013). https://doi.org/10.1103/PhysRevLett.110.112301. arXiv:1204.4442
143. I. Kuznetsova, J. Rafelski, Heavy flavor hadrons in statistical hadronization of strangeness-rich QGP. Eur. Phys. J. C **51**, 113–133 (2007). https://doi.org/10.1140/epjc/s10052-007-0268-9. arXiv:hep-ph/0607203
144. A. Andronic, P. Braun-Munzinger, K. Redlich et al., Charmonium and open charm production in nuclear collisions at SPS/FAIR energies and the possible influence of a hot hadronic medium. Phys. Lett. B **659**, 149–155 (2008). https://doi.org/10.1016/j.physletb.2007.10.064. arXiv:0708.1488
145. S.H. Lee, K. Ohnishi, S. Yasui et al., Λ_c enhancement from strongly coupled quark-gluon plasma. Phys. Rev. Lett. **100**, 222301 (2008). https://doi.org/10.1103/PhysRevLett.100.222301. arXiv:0709.3637
146. Y. Oh, C.M. Ko, S.H. Lee et al., Heavy baryon/meson ratios in relativistic heavy ion collisions. Phys. Rev. C **79**, 044905 (2009). https://doi.org/10.1103/PhysRevC.79.044905. arXiv:0901.1382
147. S.K. Das, J.M. Torres-Rincon, L. Tolos et al., Propagation of heavy baryons in heavy-ion collisions. Phys. Rev. D **94**, 114039 (2016). https://doi.org/10.1103/PhysRevD.94.114039. arXiv:1604.05666
148. S. Plumari, V. Minissale, S.K. Das et al., Charmed hadrons from coalescence plus fragmentation in relativistic nucleus-nucleus collisions at RHIC and LHC. Eur. Phys. J. C **78**, 348 (2018). https://doi.org/10.1140/epjc/s10052-018-5828-7. arXiv:1712.00730
149. M. He, R. Rapp, Hadronization and charm-hadron ratios in heavy-ion collisions. Phys. Rev. Lett. **124**, 042301 (2020). https://doi.org/10.1103/PhysRevLett.124.042301. arXiv:1905.09216
150. A. Beraudo, A. De Pace, M. Monteno et al., In-medium hadronization of heavy quarks and its effect on charmed meson and baryon distributions in heavy-ion collisions. Eur. Phys. J. C **82**, 607 (2022). https://doi.org/10.1140/epjc/s10052-022-10482-y. arXiv:2202.08732
151. A. Beraudo et al., Extraction of heavy-flavor transport coefficients in QCD matter. Nucl. Phys. A **979**, 21–86 (2018). https://doi.org/10.1016/j.nuclphysa.2018.09.002. arXiv:1803.03824
152. S. Acharya et al., Constraining hadronization mechanisms with Λ_c/D_0 production ratios in Pb-Pb collisions. Phys. Lett. B **839**, 137796 (2023). https://doi.org/10.1016/j.physletb.2023.137796. arXiv:2112.08156
153. S. Acharya et al., Λ_c production in pp and in p-Pb collisions at $\sqrt{s_{NN}} = 5$ TeV. Phys. Rev. C **104**, 054905 (2021). https://doi.org/10.1103/PhysRevC.104.054905. arXiv:2011.06079
154. S. Acharya et al., Measurement of beauty-strange meson production in Pb-Pb collisions at $\sqrt{s_{NN}} = 5$ TeV via non-prompt D_s mesons. Phys. Lett. B **846**, 137561 (2023). https://doi.org/10.1016/j.physletb.2022.137561. arXiv:2204.10386
155. M. He, R.J. Fries, R. Rapp, Heavy flavor at the large hadron collider in a strong coupling approach. Phys. Lett. B **735**, 445–450 (2014). https://doi.org/10.1016/j.physletb.2014.05.050. arXiv:1401.3817
156. L. Ravagli, R. Rapp, Quark coalescence based on a transport equation. Phys. Lett. B **655**, 126–131 (2007). https://doi.org/10.1016/j.physletb.2007.07.043. arXiv:0705.0021
157. M.L. Mangano, P. Nason, G. Ridolfi, Heavy quark correlations in hadron collisions at next-to-leading order. Nucl. Phys. B **373**, 295–345 (1992). https://doi.org/10.1016/0550-3213(92)90435-E
158. M. Cacciari, M. Greco, P. Nason, The p_T spectrum in heavy-flavour hadroproduction. JHEP **9805**, 007 (1998). https://doi.org/10.1088/1126-6708/1998/05/007. arXiv:hep-ph/9803400
159. S. Acharya et al., Charm-quark fragmentation fractions and production cross section at midrapidity in pp collisions at the LHC. Phys. Rev. D **105**, L011103 (2022). https://doi.org/10.1103/PhysRevD.105.L011103. arXiv:2105.06335
160. B.B. Abelev et al., Beauty production in pp collisions at $\sqrt{s} = 2.76$ TeV measured via semi-electronic decays. Phys. Lett. B **738**, 97–108 (2014). https://doi.org/10.1016/j.physletb.2014.09.026. arXiv:1405.4144
161. B. Abelev et al., Measurement of electrons from beauty hadron decays in pp collisions at $\sqrt{s}$ =7 TeV. Phys. Lett. B **721**, 13–23 (2013). https://doi.org/10.1016/j.physletb.2013.01.069
162. S. Acharya et al., Prompt and non-prompt J/ψ production cross sections at midrapidity in proton–proton collisions at $\sqrt{s} = 5.02$ and 13 TeV. JHEP **2203**, 190 (2022). https://doi.org/10.1007/JHEP03(2022)190. arXiv:2108.02523
163. B. Abelev et al., Heavy flavour decay muon production at forward rapidity in proton-proton collisions at $\sqrt{s} = 7$ TeV. Phys. Lett. B **708**, 265–275 (2012). https://doi.org/10.1016/j.physletb.2012.01.063. arXiv:1201.3791
164. S. Acharya et al., Production of muons from heavy-flavour hadron decays in pp collisions at $\sqrt{s} = 5.02$ TeV. JHEP **1909**, 008 (2019). https://doi.org/10.1007/JHEP09(2019)008
165. S. Acharya et al., Charm production and fragmentation fractions at midrapidity in pp collisions at $\sqrt{s} = 13$ TeV. JHEP **2312**, 086 (2023). https://doi.org/10.1007/JHEP12(2023)086. arXiv:2308.04877
166. M. Lisovyi, A. Verbytskyi, O. Zenaiev, Combined analysis of charm-quark fragmentation-fraction measurements. Eur. Phys. J. C **76**, 397 (2016). https://doi.org/10.1140/epjc/s10052-016-4246-y. arXiv:1509.01061
167. S. Acharya et al., Measurements of azimuthal anisotropies at forward and backward rapidity with muons in high-multiplicity p-Pb collisions at $\sqrt{s_{NN}} = 8.16$ TeV. Phys. Lett. B **846**, 137782 (2023). https://doi.org/10.1016/j.physletb.2023.137782. arXiv:2210.08980
168. Z.W. Lin, L. Zheng, Further developments of a multi-phase transport model for relativistic nuclear collisions. Nucl. Sci. Tech. **32**, 113 (2021). https://doi.org/10.1007/s41365-021-00944-5. arXiv:2110.02989
169. C. Zhang, C. Marquet, G.Y. Qin et al., Collectivity of heavy mesons in proton-nucleus collisions. Phys. Rev. D **102**, 034010 (2020). https://doi.org/10.1103/PhysRevD.102.034010. arXiv:2002.09878
170. J.C. Collins, D.E. Soper, G.F. Sterman, Factorization of hard processes in QCD. Adv. Ser. Direct. High Energy Phys. **5**, 1–91

(1989). https://doi.org/10.1142/9789814503266_0001. arXiv:hep-ph/0409313
171. S. Catani, M. Ciafaloni, F. Hautmann, High-energy factorization and small x heavy flavor production. Nucl. Phys. B **366**, 135–188 (1991). https://doi.org/10.1016/0550-3213(91)90055-3
172. J.C. Collins, Hard scattering factorization with heavy quarks: a general treatment. Phys. Rev. D **58**, 094002 (1998). https://doi.org/10.1103/PhysRevD.58.094002. arXiv:hep-ph/9806259
173. R.K. Ellis, W. Furmanski, R. Petronzio, Unraveling higher twists. Nucl. Phys. B **212**, 29 (1983). https://doi.org/10.1016/0550-3213(83)90597-7
174. S. Alekhin, J. Blümlein, S. Moch et al., Parton distribution functions, α_s, and heavy-quark masses for LHC Run II. Phys. Rev. D **96**, 014011 (2017). https://doi.org/10.1103/PhysRevD.96.014011. arXiv:1701.05838
175. S. Acharya et al., Λ_c production and baryon-to-meson ratios in pp and p-Pb collisions at $\sqrt{s_{\rm NN}} = 5$ TeV at the LHC. Phys. Rev. Lett. **127**, 202301 (2021). https://doi.org/10.1103/PhysRevLett.127.202301. arXiv:2011.06078
176. S. Acharya et al., Measurement of prompt $\rm D^0$, Λ_c^+, and $\Sigma_c^{0,++}$ (2455) production in proton-proton collisions at $\sqrt{s} = 13$ TeV. Phys. Rev. Lett. **128**, 012001 (2022). https://doi.org/10.1103/PhysRevLett.128.012001. arXiv:2106.08278
177. S. Acharya et al., First measurement of Ω_c^0 production in pp collisions at $\sqrt{s} = 13$ TeV. Phys. Lett. B **846**, 137625 (2023). https://doi.org/10.1016/j.physletb.2022.137625. arXiv:2205.13993
178. S. Acharya et al., Charm fragmentation fractions and $\rm c\bar{c}$ cross section in p–Pb collisions at $\sqrt{s_{\rm NN}} = 5$ TeV. arXiv:2405.14571
179. N. Armesto, Small collision systems: Theory overview on cold nuclear matter effects. EPJ Web Conf. **171**, 11001 (2018). https://doi.org/10.1051/epjconf/201817111001
180. S. Acharya et al., Measurement of prompt $\rm D^0$, $\rm D^+$, $\rm D^{*+}$, and D_s production in p-Pb collisions at $\sqrt{s_{\rm NN}} = 5$ TeV. JHEP **1912**, 092 (2019). https://doi.org/10.1007/JHEP12(2019)092. arXiv:1906.03425
181. S. Acharya et al., First measurement of Λ_c production down to $p_T = 0$ in pp and p-Pb collisions at $\sqrt{s_{\rm NN}} = 5$ TeV. Phys. Rev. C **107**, 064901 (2023). https://doi.org/10.1103/PhysRevC.107.064901. arXiv:2211.14032
182. S. Acharya et al., Measurement of the production cross section of prompt Ξ_c^0 baryons in p–Pb collisions at $\sqrt{s_{\rm NN}} = 5$ TeV. arXiv:2405.14538
183. S. Acharya et al., $\rm W^{\pm}$-boson production in p-Pb collisions at $\sqrt{s_{\rm NN}} = 8.16$ TeV and Pb–Pb collisions at $\sqrt{s_{\rm NN}} = 5$ TeV. JHEP **2305**, 036 (2023). https://doi.org/10.1007/JHEP05(2023)036. arXiv:2204.10640
184. J. Adam et al., Measurement of electrons from beauty-hadron decays in p-Pb collisions at $\sqrt{s_{\rm NN}} = 5$ TeV and Pb–Pb collisions at $\sqrt{s_{\rm N}} = 2.76$ TeV. JHEP **1707**, 052 (2017). https://doi.org/10.1007/JHEP07(2017)052. arXiv:2204.10640
185. S. Acharya et al., Measurement of inclusive charged-particle b-jet production in pp and p-Pb collisions at $\sqrt{s_{\rm NN}} = 5$ TeV. JHEP **2201**, 178 (2022). https://doi.org/10.1007/JHEP01(2022)178. arXiv:2110.06104
186. S. Acharya et al., Azimuthal anisotropy of heavy-flavor decay electrons in p-Pb collisions at $\sqrt{s_{\rm NN}} = 5$ TeV. Phys. Rev. Lett. **122**, 072301 (2019). https://doi.org/10.1103/PhysRevLett.122.072301. arXiv:1805.04367
187. S. Acharya et al., Measurement of the radius dependence of charged-particle jet suppression in Pb-Pb collisions at $\sqrt{s_{\rm NN}} = 5.02$ TeV. Phys. Lett. B **849**, 138412 (2024). https://doi.org/10.1016/j.physletb.2023.138412
188. S. Acharya et al., Modification of charged-particle jets in event-shape engineered Pb–Pb collisions at $\sqrt{s_{\rm NN}} = 5.02$ TeV. Phys. Lett. B **851**, 138584 (2024). https://doi.org/10.1016/j.physletb.2024.138584
189. S. Acharya, D. Adamová, G. Aglieri Rinella et al., Measurements of jet quenching using semi-inclusive hadron+jet distributions in pp and central Pb-Pb collisions at $\sqrt{s_{\rm NN}} = 5.02$ TeV. Phys. Rev. C **110**, 014906 (2024). https://doi.org/10.1103/PhysRevC.110.014906
190. S. Acharya, D. Adamová, G. Aglieri Rinella et al., Observation of medium-induced yield enhancement and acoplanarity broadening of low-$p_{\rm t}$ jets from measurements in pp and central Pb-Pb collisions at $\sqrt{s_{\rm NN}} = 5.02$ TeV. Phys. Rev. Lett. **133**, 022301 (2024). https://doi.org/10.1103/PhysRevLett.133.022301
191. S. Acharya et al., Multiplicity dependence of charged-particle jet production in pp collisions at $\sqrt{s} = 13$ TeV. Eur. Phys. J. C **82**, 514 (2022). https://doi.org/10.1140/epjc/s10052-022-10405-x
192. S. Acharya et al., Search for jet quenching effects in high-multiplicity pp collisions at $\sqrt{s} = 13$ TeV via di-jet acoplanarity. J. High Energy Phys. **2024**, 229 (2024). https://doi.org/10.1007/JHEP05(2024)229
193. Measurement of the angle between jet axes in Pb–Pb collisions at $\sqrt{s_{\rm NN}} = 5.02$ TeV. (2023). arXiv:2303.13347
194. S. Acharya et al., Direct observation of the dead-cone effect in quantum chromodynamics. Nature **605**, 440–446 (2022). https://doi.org/10.1038/s41586-022-04572-w
195. L. Musa, Letter of intent for an ALICE ITS upgrade in LS3. https://doi.org/10.17181/CERN-LHCC-2019-018
196. Letter of intent: a forward calorimeter (focal) in the ALICE experiment. (2020) https://cds.cern.ch/record/2719928
197. Upgrade of the ALICE inner tracking system during LS3: study of physics performance. (2023) https://cds.cern.ch/record/2868015
198. Physics performance of the ALICE forward calorimeter upgrade. (2023) https://cds.cern.ch/record/2869141
199. Technical design report for the ALICE inner tracking system 3 - its3 ; a bent wafer-scale monolithic pixel detector. (2024) https://cds.cern.ch/record/2890181
200. Technical design report of the ALICE forward calorimeter (FoCal). (2024) https://cds.cern.ch/record/2890281
201. Letter of intent for ALICE 3: a next-generation heavy-ion experiment at the LHC. (2022). arXiv:2211.02491